

The Complete Local Volume Groups Sample - II. A study of the Central Radio Galaxies in the High-Richness Sub-sample

Konstantinos Kolokythas,^{1*} Ewan O’Sullivan,² Somak Raychaudhury,^{1,3}
Simona Giacintucci,⁴ Myriam Gitti,^{5,6} Arif Babul^{7,8}

¹Inter-University Centre for Astronomy and Astrophysics, Pune University Campus, Ganeshkhind, Pune, Maharashtra 411007, India

²Harvard-Smithsonian Center for Astrophysics, 60 Garden Street, Cambridge, MA 02138, USA

³School of Physics and Astronomy, University of Birmingham, Birmingham B15 2TT, UK

⁴Naval Research Laboratory, 4555 Overlook Avenue SW, Code 7213, Washington, DC 20375, USA

⁵Dipartimento di Fisica e Astronomia, Università di Bologna, via Gobetti 93/2, 40129 Bologna, Italy

⁶INAF, Istituto di Radioastronomia di Bologna, via Gobetti 101, 40129 Bologna, Italy

⁷Department of Physics and Astronomy, University of Victoria, Victoria, BC V8P 1A1, Canada

⁸Center for Theoretical Astrophysics and Cosmology, Institute for Computational Science, University of Zurich, Winterthurerstrasse 190, 8057 Zurich, Switzerland

Accepted 2018 July 26; Received 2018 July 17; in original form 2018 April 11

ABSTRACT

We present a study of the radio properties of the dominant early-type galaxies in 26 galaxy groups, the high-richness sub-sample of the Complete Local-volume Groups Sample (CLoGS). Combining new 610 MHz and 235 MHz observations of 21 groups from the Giant Metrewave Radio Telescope (GMRT) with archival GMRT and Very Large Array (VLA) survey data, we find a high detection rate, with 92% of the dominant galaxies hosting radio sources. The sources have a wide range of luminosities, $10^{20} - 10^{24}$ W Hz⁻¹ in the 235 and 610 MHz bands. The majority (54%) are point-like, but 23% have radio jets, and another 15% are diffuse radio sources with no clear jet/lobe morphology. Star formation may dominate the radio emission in 2 of the point-like systems and may make a significant contribution to a further 1–3, but is unlikely to be important in the remaining 21 galaxies. The spectral index of the detected radio sources ranges from very flat values of ~ 0.2 to typical radio synchrotron spectra of ~ 0.9 with only two presenting steep radio spectra with $\alpha_{235}^{610} > 1$. We find that jet sources are more common in X-ray bright groups, with radio non-detections found only in X-ray faint systems. Radio point sources appear in all group environments irrespective of their X-ray properties or spiral fraction. We estimate the mechanical power (P_{cav}) of the jet sources in the X-ray bright groups to be $10^{41} - 10^{43}$ erg s⁻¹, with the two large-scale jet systems (NGC 193 and NGC 4261) showing jet powers two orders of magnitude greater than the radiative losses from the cool cores of their groups. This suggests that central AGN are not always in balance with cooling, but may instead produce powerful periodical bursts of feedback heating.

Key words: galaxies: groups: general — galaxies: active — galaxies: jets — radio continuum: galaxies

1 INTRODUCTION

Much of the evolution of galaxies takes place in the group environment. Despite the small number of galaxies a typical group contains compared to a cluster, the role of galaxy groups in the construction of large-scale structures is fundamental. With approximately 70% of galaxies located in groups (Tully 1987), they are the most common environment in the local Universe (Geller & Huchra 1983; Eke et al. 2005). In hierarchical structure formation, galaxy clusters

are built up through the merger of groups (e.g. van den Bosch et al. 2014; Haines et al. 2017), and the early evolution of rich cluster galaxies (e.g. Bekki et al. 1999; Moss & Whittle 2000) is thus closely connected with the evolution of galaxies in groups. The study of groups is therefore essential in order to acquire a complete understanding of the evolution of galaxies along with the environmental processes involved (e.g. Forbes et al. 2006).

Galaxy groups are an ideal laboratory to study the most efficient process in the morphological transformation of galaxies: merging (e.g. Toomre & Toomre 1972). Mamon (2000) showed that galaxies in groups merge roughly two orders of magnitude

* e-mail: kkolok@iucaa.in

more often than in rich clusters. Although groups represent shallower potential wells, gravity plays an important role due to the low velocity dispersion of these systems and the close proximity of members. The high rate of mergers and tidal interactions makes the group environment a locus of galaxy evolution and enhanced star formation (e.g., Mulchaey & Zabludoff 1998; Hashimoto & Oemler 2000).

Many galaxy groups also possess hot gaseous haloes which, given the ubiquity of groups, make up a significant fraction of the baryonic component of the Universe (Fukugita et al. 1998). However, whereas in virialised clusters the hot gas is always the dominant baryonic component, in groups the gas content varies, with numerous examples of systems in which the gas and stellar components are equal (Laganá et al. 2011) or in which the stellar component dominates (e.g. Giodini et al. 2009). Hence, groups are the natural environment to study the origin and nature of this important mass component and its close relationship with galaxies and their evolution (Forbes et al. 2006; Liang et al. 2016).

One aspect of this relationship which is of particular interest is the thermal regulation of the intra-group medium (IGM) via star formation or active galactic nuclei (AGN) fuelled by cooling gas (generally referred to as ‘feedback’). The most common observational evidence for the AGN mechanism are the radio bubbles and the X-ray cavities that the radio galaxies create in the hot IGM or the gaseous haloes of their host galaxies (McNamara et al. 2000; Fabian et al. 2006). While many studies have focused on the most powerful AGN in massive clusters of galaxies (e.g., McNamara et al. 2005), groups of galaxies are an important environment, where feedback may have the greatest impact on galaxy evolution and formation.

Like the brightest cluster galaxies (BCGs), brightest group-dominant early-type galaxies (BGEs) are ideal targets for the study of the evolution of groups and massive galaxies. They are typically highly luminous, old elliptical galaxies, located near the centres of the IGM and dark matter halo (e.g., von der Linden et al. 2007; Stott et al. 2010). Their stellar kinematic properties cover the full range from field elliptical-like to BCG-like (Loubser et al. 2018) and their nuclei host super-massive black holes (e.g. Rafferty et al. 2006), with many of the BGEs revealing the activity of their nuclei by radio emission and even with radio jets that deposit their energy back to the IGM (see McNamara & Nulsen 2007).

Earlier studies have shown that $\sim 30\%$ of the most massive galaxies exhibit radio continuum emission (e.g., Best et al. 2005; Shabala et al. 2008), with relevant group/cluster studies of central BGEs/BCGs in the local Universe suggesting a high detection rate (80-90%) in radio (e.g., Magliocchetti & Brüggén 2007; Dunn et al. 2010). It is also known that radio AGN in early-type galaxies are more common in higher density environments (groups or clusters; Lilly et al. 2009; Bardelli et al. 2010; Malavasi et al. 2015). In such environments, the radio activity in cluster and group-central AGN is most effectively enhanced by cluster/group merging, or in the case of lower density environments by ‘inter-group’ galaxy-galaxy interactions and mergers (Miles et al. 2004; Taylor & Babul 2005). It appears that mergers and interactions direct gas to the AGN in early type galaxies, resulting in radio emission and the launching of jets, whereas in late-type galaxies, the corresponding processes would trigger or increase radio emission from star formation (SF) (e.g., Vollmer et al. 2001).

Galaxy clusters may also host diffuse structures associated with the ICM (see Kempner et al. 2004, for a general classification of cluster radio sources). These include *mini-halos*, typically found at the center of cool-core clusters around powerful radio galaxies,

and thought to be powered by turbulence in the cooling region or perhaps by minor mergers (Ferrari et al. 2008; Feretti et al. 2012; Brunetti & Jones 2014; Gitti et al. 2015; Giacintucci et al. 2017), *radio relics*, narrow, linear arcs of radio emission found far from the cluster core, associated with large-scale shocks and steep spectral indices, and *radio halos*, which are thought to be produced through turbulent re-acceleration of electrons by a cluster merger event. In galaxy groups the diffuse radio sources seen are mainly associated with the central galaxy and not the IGM but their production mechanism is still uncertain.

In this paper we present a study of the radio properties of the dominant galaxies of the 26-group CLoGS high-richness subsample, including new Giant Metrewave Radio Telescope (GMRT) 235 and 610 MHz observations of 21 systems. We present the properties of the central radio sources, examine their environment and provide qualitative comparison between the GMRT radio data and the X-ray data for each group. The CLoGS sample and the X-ray properties of the groups are described in more detail in O’Sullivan et al. (2017, hereafter Paper I). The paper is organized as follows: In Section 2 we present the sample of galaxy groups, whereas, in Section 3 we describe the GMRT and X-ray observations along with the approach followed for the radio data reduction. In Section 4 we present the radio detection statistics of the BGEs, and in Section 5 their radio properties (morphology and power) along with information on their spectral index and the possible contribution from star formation on their radio emission. Section 6 contains the discussion of our results focusing on detection statistics, environmental properties of the radio sources and the energetics of jet systems with cavities. The summary and the conclusions are given in Section 7. The radio images and information on the central galaxies of this sample work are presented in Appendix A, the values of star formation rates (SFR_{FUV}) and expected radio power due to star formation for the related BGEs are shown in Appendix B and the information on the flux density distribution for each system is given in Appendix C. Throughout the paper we adopt the Λ CDM cosmology with $H_o = 71 \text{ km s}^{-1} \text{ Mpc}^{-1}$, $\Omega_m = 0.27$, and $\Omega_\Lambda = 0.73$. The radio spectral index α is defined as $S_\nu \propto \nu^{-\alpha}$, where S_ν is the flux density at the frequency ν .

2 THE COMPLETE LOCAL-VOLUME GROUPS SAMPLE

We present in this section only a short general description of the Complete Local-Volume Groups Sample (CLoGS). CLoGS is an optically-selected, statistically-complete sample of groups in the nearby universe, chosen to facilitate studies in the radio, X-ray and optical bands, with the detection of an X-ray luminous IGM providing confirmation that groups are gravitationally bound systems. The sample is intended to facilitate investigations of a number of scientific questions, including the role of AGNs in maintaining the thermal balance of the IGM.

A detailed description of the CLoGS sample selection criteria and the X-ray properties of the high-richness subsample can be found in Paper I. CLoGS is an optically selected sample of 53 groups in the local Universe ($\leq 80 \text{ Mpc}$), drawn from the shallow, all-sky Lyon Galaxy Group catalog sample (LGG; Garcia 1993). Groups were selected to have a minimum of 4 members and at least one luminous early-type galaxy ($L_B > 3 \times 10^{10} L_\odot$). Declination was required to be $> 30^\circ$ to ensure visibility from the GMRT and Very Large Array (VLA).

Group membership was expanded and refined using the Hy-

perLEDA catalog (Paturel et al. 2003), and group mean velocity dispersion and richness R were estimated from the revised membership, where richness is defined as the number of member galaxies with $\log L_B \geq 10.2$. Systems with $R > 10$ correspond to known galaxy clusters and were excluded, as were six groups that have $R = 1$, since they are not rich enough to give a trustworthy determination of their physical parameters. This selection process produced a 53-group statistically complete sample, which we then divided into two sub-samples: i) the 26 high-richness groups with $R = 4-8$ and ii) the 27 low-richness groups $R = 2-3$. The BGE was assumed to lie at or near the centre of the group, and used as the target for observations. In this paper we examine the radio properties of the high-richness sub-sample.

3 OBSERVATIONS AND DATA ANALYSIS

3.1 GMRT radio observations and data analysis

With the exception of systems for which suitable archival data was already available, the CLoGS galaxy groups were observed using the GMRT in dual-frequency 235/610 MHz mode during 2010 December, 2011 April, July and November, 2012 March and 2013 October. The average total time spent on each source was approximately 4 hours. The data for both frequencies were recorded using the upper side band correlator (USB) providing a total observing bandwidth of 32 MHz at both 610 and 235 MHz. The data for both frequencies were collected with 512/256 channels at a spectral resolution of 65.1/130.2 kHz per channel and were analysed and reduced using the NRAO Astronomical Image Processing System (AIPS) package. In Table 1 we summarize the details of the observations, where we report the observing date, frequency, total time on source, the half-power beamwidth (HPBW) and the rms noise level (1σ) at full resolution.

The procedure of the GMRT data analysis followed is the same as described in Kolokythas et al. (2015). The data were edited to remove radio-frequency interference (RFI) by initially removing data with extreme phase difference from the phase and flux calibrators, and then from the source. The task SETJY was used and the flux density scale was set to “best VLA values (2010)¹”. The data were then calibrated using the task CALIB using uniform weighting, and the flux density scale was defined using the amplitude calibrators observed at the beginning and end at each of our observations. Then a calibrated, RFI-free channel was used for bandpass calibration, in order to relate the amplitude difference between all channels. Using task SPLAT, the channels were averaged in order to increase signal-to-noise while minimizing the effects of band smearing.

For imaging purposes, the field of view of the GMRT was split into multiple facets approximating a plane surface in the imaging field. The normal number of facets created at 610 MHz was 56 (with cellsize $1.5''$) and 85 at 235 MHz (with cellsize $3''$). The final images give a field of view of $\sim 1.2^\circ \times 1.2^\circ$ at 610 MHz and $\sim 3^\circ \times 3^\circ$ at 235 MHz. Task IMAGR was then used repeatedly, applying phase-only self-calibration before every iteration. The majority of the noise remaining in our images arises from calibration uncertainties with phase errors at the lowest frequencies originating from rapidly varying ionospheric delays. The presence of bright sources in the field can also affect the noise level in our final images, reducing the dynamic range.

The final images were corrected for the primary beam pattern of the GMRT using the task PBCOR. The mean sensitivity (1σ noise level) of the analysis achieved in the final full resolution images is ~ 0.08 mJy at 610 MHz and ~ 0.6 mJy at 235 MHz (see Table 1). The theoretical values of noise calculated for our observations are $29 \mu\text{Jy}$ for 610 MHz and $80 \mu\text{Jy}$ for 235 MHz². The mean sensitivity achieved for 610 MHz is comparable to the theoretical noise level while at 235 MHz the mean sensitivity is considerably higher than the theoretical level. We note that the full resolution of the GMRT is $\sim 13''$ at 235 MHz and $\sim 6''$ at 610 MHz with the $u-v$ range at 235 MHz being $\sim 0.05 - 21$ k λ and $\sim 0.1 - 50$ k λ at 610 MHz. The error associated with the flux density measurements is the typical uncertainty in the residual amplitude calibration errors. That is $\sim 5\%$ at 610 MHz and $\sim 8\%$ at 235 MHz (e.g., Chandra et al. 2004).

Out of the 26 BGEs in the CLoGS high-richness sub-sample, 20 were analyzed in this study at both GMRT 610/235 MHz and one (NGC 5846) at 235 MHz. The GMRT observations and images for NGC 193, NGC 7619, NGC 1587 at both 235/610 MHz and NGC 5846 at 610 MHz, are drawn from the earlier study of Giacintucci et al. (2011), those for NGC 5044 from David et al. (2009, 2011) and for NGC 4261 from Kolokythas et al. (2015). Analysis of those observations is described in detail in those works. For sources with resolved structure at both GMRT frequencies (see Table 6), we created spectral index maps using the task COMB in AIPS with images having the same uv range, resolution and cellsize. 1400 MHz data were drawn primarily from the NRAO VLA Sky Survey (NVSS, Condon et al. 1998) and the Faint Images of the Radio Sky at Twenty centimeters Survey (FIRST, Becker et al. 1995). For some sources, flux densities were drawn from Brown et al. (2011), who used measurements from the NVSS, Green Bank Telescope, and Parkes Radio Telescope, as well as from Kuhr et al. (1981) and Condon et al. (2002) studies for NGC 4261 and NGC 193 respectively.

3.2 X-ray observations

Paper I describes the X-ray properties of the high-richness group sample, based on observations from the *Chandra* and *XMM-Newton* observatories. We summarize here only the main results of the X-ray analysis, as our focus is the comparison between the radio and X-ray structures.

Of the 26 groups of the high-richness sub-sample, 19 were observed by *XMM-Newton*, 13 by *Chandra*, and 8 have data from both X-ray observatories. An IGM is detected in 14/26 systems ($\sim 54\%$) with a further 3/26 systems ($\sim 12\%$) containing galaxy-scale haloes of X-ray emitting gas (extent < 65 kpc, luminosity $< 10^{41}$ erg s⁻¹) associated with the dominant early-type galaxy. The remaining nine groups show only point-like X-ray emission ($\sim 35\%$) from AGN and stellar sources in member galaxies. In the groups with detected gas haloes, the typical halo temperatures are found to be in the range $\sim 0.4 - 1.4$ keV, corresponding to masses in the range $M_{500} \sim 0.5 - 5 \times 10^{13} M_\odot$. The X-ray luminosities of the systems were estimated in the 0.5 – 7 keV band to be between $L_{X,R500} \sim 2 - 200 \times 10^{41}$ erg s⁻¹. Paper I classes systems that have a central decline in their X-ray temperature profile (at greater than 3σ significance) as cool core. By this definition, roughly one

¹ <http://www.vla.nrao.edu/astro/calib/manual/baars.html>

² Calculated using the rms noise sensitivity equation in §2.1.6 from the GMRT Observer’s Manual: http://gmrt.nrao.tifr.res.in/gmrt_hpape/Users/doc/manual/Manual_2013/manual_20Sep2013.pdf

Table 1. Details of our GMRT observations analysed here, along with information on data used in the previous study of Giacintucci et al. (2011) and David et al. (2009). For each source the first line displays the details for the 610 MHz and the second line for the 235 MHz. The columns give the LGG (Lyon Groups of Galaxies) number for each group, the BGE name, observation date, frequency, time on source, beam parameters and the rms noise in the resulting images.

| Group Name LGG | BGE | Observation Date | Frequency (MHz) | On source Time (minutes) | Beam, P.A. (Full array, "×", °) | rms mJy beam ⁻¹ |
|-------------------|-----------------------|---------------------|--------------------|-----------------------------|------------------------------------|-------------------------------|
| 18 | NGC 410 | 2011 Jul | 610 | 218 | 6.97 × 4.09, 71.48 | 0.05 |
| | | 2011 Jul | 235 | 218 | 17.87 × 10.95, 50.40 | 0.40 |
| 27 | NGC 584 | 2011 Jul | 610 | 200 | 6.82 × 3.22, 59.80 | 0.20 |
| | | 2011 Jul | 235 | 200 | 17.87 × 10.95, 50.40 | 1.20 |
| 31 | NGC 677 | 2013 Oct | 610 | 200 | 5.26 × 4.34, 68.59 | 0.04 |
| | | 2013 Oct | 235 | 200 | 12.94 × 10.76, 66.90 | 1.20 |
| 42 | NGC 777 | 2010 Dec | 610 | 338 | 5.71 × 4.76, -70.53 | 0.15 |
| | | 2010 Dec | 235 | 338 | 12.96 × 19.94, 65.78 | 0.40 |
| 58 | NGC 940 | 2010 Dec | 610 | 360 | 5.81 × 4.76, -75.11 | 0.06 |
| | | 2010 Dec | 235 | 360 | 13.27 × 11.16, 66.88 | 0.30 |
| 61 | NGC 924 | 2011 Jul | 610 | 125 | 5.52 × 3.74, 56.25 | 0.05 |
| | | 2011 Jul | 235 | 125 | 12.40 × 10.43, 59.19 | 0.30 |
| 66 | NGC 978 | 2010 Dec | 610 | 341 | 5.81 × 4.65, -81.63 | 0.06 |
| | | 2010 Dec | 235 | 341 | 14.13 × 11.69, 76.74 | 0.40 |
| 72 | NGC 1060 | 2010 Dec | 610 | 286 | 3.97 × 3.54, -86.98 | 0.09 |
| | | 2010 Dec | 235 | 286 | 13.97 × 11.87, 81.36 | 0.50 |
| 80 | NGC 1167 | 2011 Jul | 610 | 139 | 7.41 × 4.04, 68.27 | 0.06 |
| | | 2011 Jul | 235 | 139 | 16.08 × 10.40, 66.80 | 0.6 |
| 103 | NGC 1453 | 2011 Nov | 610 | 187 | 7.99 × 4.60, 48.98 | 0.06 |
| | | 2013 Oct | 235 | 258 | 16.06 × 11.34, 58.47 | 0.60 |
| 158 | NGC 2563 | 2010 Dec | 610 | 344 | 5.10 × 4.60, -57.85 | 0.07 |
| | | 2010 Dec | 235 | 344 | 11.88 × 9.93, 53.00 | 0.30 |
| 185 | NGC 3078 | 2010 Dec | 610 | 369 | 6.61 × 4.71, 2.38 | 0.20 |
| | | 2010 Dec | 235 | 369 | 16.02 × 10.99, 20.72 | 0.50 |
| 262 | NGC 4008 | 2011 Apr | 610 | 168 | 5.76 × 4.52, 78.93 | 0.05 |
| | | 2011 Apr | 235 | 168 | 14.38 × 11.78, 89.31 | 1.30 |
| 276 | NGC 4169 | 2011 Apr | 610 | 168 | 5.47 × 4.43, 61.96 | 0.08 |
| | | 2011 Apr | 235 | 168 | 13.94 × 10.78, 72.62 | 1.20 |
| 278 | NGC 4261 | 2009 Feb | 610 | 270 | 7.32 × 4.77, 76.62 | 1.00 |
| | | 2009 Feb | 235 | 270 | 15.30 × 11.00, 67.17 | 1.60 |
| 310 | ESO 507-25 | 2011 Apr | 610 | 167 | 9.40 × 8.43, 2.59 | 0.10 |
| | | 2011 Apr | 235 | 167 | 15.59 × 12.22, 7.69 | 0.50 |
| 345 | NGC 5084 | 2011 Jul | 610 | 150 | 5.91 × 5.06, 29.68 | 0.09 |
| | | 2011 Jul | 235 | 150 | 15.71 × 12.62, -4.35 | 0.65 |
| 351 | NGC 5153 | 2011 Apr | 610 | 167 | 7.63 × 4.81, 26.32 | 0.06 |
| | | 2011 Apr | 235 | 167 | 16.01 × 11.25, 13.68 | 0.30 |
| 363 | NGC 5353 | 2011 Apr | 610 | 207 | 5.92 × 4.44, -76.02 | 0.06 |
| | | 2011 Apr | 235 | 207 | 16.91 × 12.00, -79.87 | 0.60 |
| 393 | NGC 5846 | 2012 Mar | 235 | 145 | 14.02 × 11.27, 85.70 | 0.50 |
| 402 | NGC 5982 | 2011 Apr | 610 | 237 | 7.99 × 6.47, -81.04 | 0.09 |
| | | 2011 Apr | 235 | 237 | 19.42 × 14.43, -63.66 | 0.40 |
| 421 | NGC 6658 | 2011 Apr | 610 | 236 | 5.03 × 4.35, 55.03 | 0.05 |
| | | 2011 Apr | 235 | 236 | 12.82 × 10.30, 69.71 | 0.60 |
| Previous work | | | | | | |
| 9 | NGC 193 ^a | 2007 Aug | 610 | 110 | 7.0 × 6.0, 0 | 0.08 |
| | | 2008 Aug | 235 | 120 | 13.5 × 12.9, -55 | 0.80 |
| 117 | NGC 1587 ^a | 2006 Aug | 610 | 200 | 5.7 × 4.7, 67 | 0.05 |
| | | 2008 Aug | 235 | 120 | 17.2 × 11.0, 46 | 1.00 |
| 338 | NGC 5044 ^b | 2008 Feb | 610 | 130 | 6.2 × 4.4, 41.9 | 0.10 |
| | | 2008 Feb | 235 | 140 | 15.9 × 11.3, -4.6 | 0.80 |
| 393 | NGC 5846 ^a | 2006 Aug | 610 | 140 | 6.0 × 5.5, -84 | 0.06 |
| 473 | NGC 7619 ^a | 2007 Aug | 610 | 100 | 6.1 × 4.6, 39 | 0.10 |
| | | 2008 Aug | 235 | 120 | 34.6 × 11.3, -41.4 | 1.20 |

^a Giacintucci et al. (2011)

^b David et al. (2009)

third (5/14) of the X-ray confirmed groups are non-cool-core systems, while the remaining two thirds (9/14) have a cool core.

Cavities in the IGM, associated with the activity of central radio jet sources, have been identified in four systems (see e.g., David et al. 2009, 2011, 2017 for NGC 5044, Allen et al. 2006, Dong et al. 2010 and Machacek et al. 2011 for NGC 5846, Bogdan et al. 2014 for NGC 193, O’Sullivan et al. 2011 for NGC 4261). In this paper, we use cavity properties to examine the power output of AGN jets. Where necessary, cavity power estimates are made using methods similar to those described in O’Sullivan et al. (2011). The cooling luminosity (L_{cool}), defined as the luminosity of the gas in the volume within which the cooling time is ≤ 3 Gyr, was calculated in the 0.5-7 keV band, based on the luminosity and cooling time profiles measured in Paper I, using a PROJECT*WABS*APEC model in XSPEC.

4 RADIO DETECTIONS IN BRIGHTEST GROUP GALAXIES

Using the 235 and 610 MHz GMRT images, and the available NVSS and FIRST catalog data, we identified sources in the BGE of each high-richness group, determined their morphology and measured their flux densities and extent. Measured flux densities are shown in Table 2. GMRT images of the groups and more details of these sources are presented in Appendix A.

We find a high radio detection rate of 92% (24 of 26 BGEs), with only two galaxies (NGC 5153 and NGC 6658) being undetected at 235, 610 and 1400 MHz. Considering only the GMRT data, 23 of the 26 BGEs are detected at 235 and/or 610 MHz (89%), with NGC 584 being the only galaxy detected at 1.4 GHz alone. In Figure 1, we present the flux density distribution at 610 MHz and 235 MHz. The majority of the BGEs have flux densities in the range 10 – 100 mJy with the flux density distribution at 610 MHz exhibiting a narrow sharp peak compared to the 235 MHz where the spread in flux densities is bigger.

We estimate the limiting sensitivity of our sample based on the typical noise level of our observations and the maximum distance for the observed groups, 78 Mpc. We define radio sources as detected in our GMRT data if they reach a 5σ level of significance above the noise. Using the mean r.m.s. from our GMRT observations for each frequency ($\sim 80 \mu\text{Jy beam}^{-1}$ at 610 MHz and $\sim 600 \mu\text{Jy beam}^{-1}$ at 235 MHz), we find that we should be sensitive to any source with power $> 2.9 \times 10^{20} \text{ W Hz}^{-1}$ at 610 MHz or $> 2.2 \times 10^{21} \text{ W Hz}^{-1}$ at 235 MHz. For comparison, the equivalent limit for NVSS 1400 MHz power sensitivity at this distance and level of significance is $> 1.7 \times 10^{21} \text{ W Hz}^{-1}$. We note that sources in nearby groups may be detected at $> 5\sigma$ significance with lower powers; these limits reflect the sensitivity of the sample as a whole.

5 RADIO PROPERTIES OF THE BRIGHTEST GROUP GALAXIES

5.1 Radio morphology

The radio-detected BGEs of the CLoGS high-richness sample exhibit a rich variety of structures that differ dramatically in size, radio power and morphology. The physical scale of their radio emission ranges from a few kpc (point sources; galactic scale) to several tens of kpc (large jets; group scale). The radio structures observed

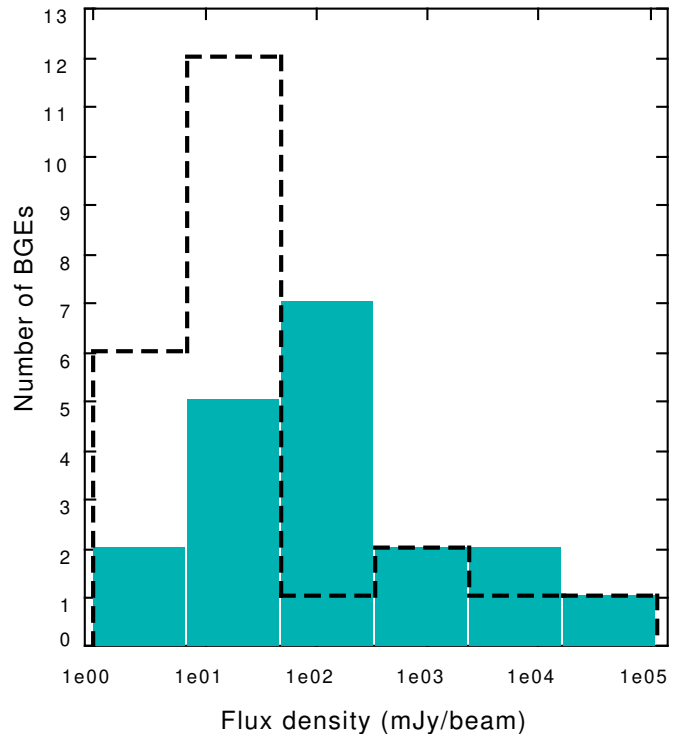


Figure 1. Flux density distribution of the central brightest group early-type galaxies of the high-richness sample at 610 MHz (black dashed line) and 235 MHz (cyan columns) in CLoGS high-richness sample.

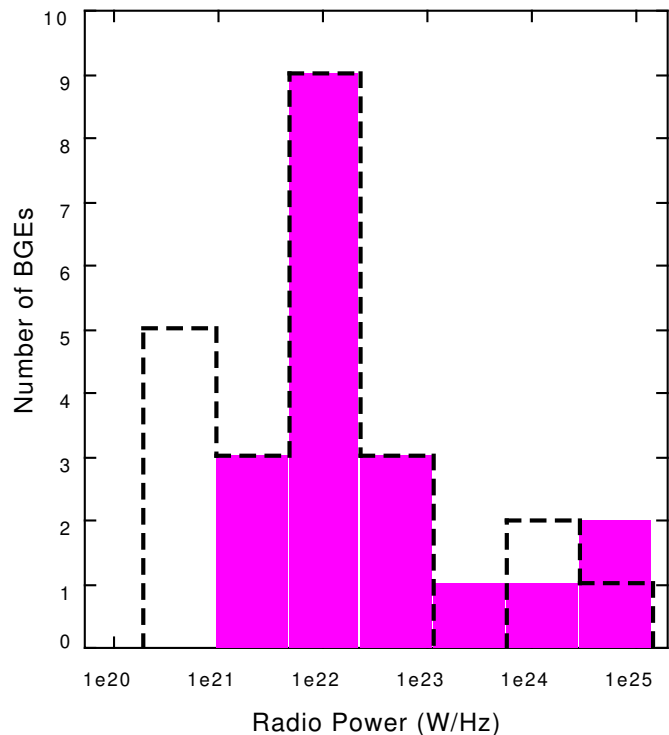


Figure 2. Radio power of the detected BGEs at 610 MHz (black dashed line) and 235 MHz (pink columns) in CLoGS high-richness sample.

Table 2. Radio flux densities and spectral indices for our targets. The columns list the BGE name, redshift, flux density of each source at 235 and 610 MHz, the 235–610 MHz spectral index, the flux density at 1.4 GHz (drawn from the literature), the 235–1400 MHz spectral index, and the radio power at 235 and 610 MHz. All upper limits shown here from our analysis are $5 \times$ r.m.s. Three galaxies show no radio emission detected from our GMRT observations. The sensitivity of the GMRT observations is on average $\sim 80 \mu\text{Jy beam}^{-1}$ at 610 MHz and $\sim 600 \mu\text{Jy beam}^{-1}$ at 235 MHz. The references for the 1.4 GHz flux densities and the GMRT measurements from previous works are listed at the bottom of the table.

| Source | Redshift (z) | $S_{235\text{MHz}}$ $\pm 8\%$ (mJy) | $S_{610\text{MHz}}$ $\pm 5\%$ (mJy) | $\alpha_{235\text{MHz}}^{610\text{MHz}}$ (± 0.04) | $S_{1.4\text{GHz}}$ (mJy) | $\alpha_{235\text{MHz}}^{1400\text{MHz}}$ | $P_{235\text{MHz}}$ ($10^{23} \text{ W Hz}^{-1}$) | $P_{610\text{MHz}}$ ($10^{23} \text{ W Hz}^{-1}$) |
|-----------------------|---------------------|--|--|--|------------------------------|---|--|--|
| NGC 410 | 0.017659 | 28.5 | 13.6 | 0.78 | 6.3 ± 0.6^a | 0.85 ± 0.05 | 0.201 | 0.096 |
| NGC 584 | 0.006011 | ≤ 6.0 | ≤ 1.0 | - | 0.6 ± 0.5^b | - | - | - |
| NGC 677 | 0.017012 | 99.2 | 45.6 | 0.81 | 20.6 ± 1.6^a | 0.88 ± 0.05 | 0.720 | 0.331 |
| NGC 777 | 0.016728 | 20.9 | 10.2 | 0.75 | 7.0 ± 0.5^b | 0.61 ± 0.05 | 0.133 | 0.065 |
| NGC 940 | 0.017075 | 3.3 | 4.3 | -0.28 | - | - | 0.021 | 0.028 |
| NGC 924 | 0.014880 | ≤ 1.5 | 1.7 | - | - | - | - | 0.008 |
| NGC 978 | 0.015794 | ≤ 2.0 | 1.3 | - | - | - | - | 0.007 |
| NGC 1060 | 0.017312 | 28.5 | 12.4 | 0.87 | 9.2 ± 0.5^b | 0.63 ± 0.04 | 0.197 | 0.086 |
| NGC 1167 | 0.016495 | 4018.4 | 2295.3 | 0.59 | 1700 ± 100^b | 0.48 ± 0.04 | 24.751 | 14.138 |
| NGC 1453 | 0.012962 | 47.1 | 40.4 | 0.16 | 28.0 ± 1^b | 0.29 ± 0.04 | 0.221 | 0.190 |
| NGC 2563 | 0.014944 | ≤ 1.5 | 1.3 | - | 0.3 ± 0.5^b | - | - | 0.007 |
| NGC 3078 | 0.008606 | 582.8 | 384.5 | 0.44 | 310 ± 10^b | 0.35 ± 0.04 | 0.802 | 0.529 |
| NGC 4008 | 0.012075 | 24.8 | 16.4 | 0.43 | 10.9 ± 0.5^b | 0.46 ± 0.04 | 0.086 | 0.057 |
| NGC 4169 | 0.012622 | ≤ 6.0 | 3.0 | - | 1.07 ± 0.15^c | - | - | 0.007 |
| NGC 4261 ^d | 0.007465 | 48500 | 29600 | 0.52 | 19510 ± 410^e | 0.51 ± 0.04 | 59.193 | 36.126 |
| ESO 507-25 | 0.010788 | 55.2 | 46.6 | 0.18 | 24.0 ± 2^b | 0.47 ± 0.05 | 0.133 | 0.112 |
| NGC 5084 | 0.005741 | 53.9 | 36.2 | 0.42 | 46.6 ± 1.8^a | 0.08 ± 0.04 | 0.034 | 0.023 |
| NGC 5153 | 0.014413 | ≤ 1.5 | ≤ 0.3 | - | - | - | - | - |
| NGC 5353 | 0.007755 | 65.8 | 45.8 | 0.38 | 41.0 ± 1.3^a | 0.27 ± 0.04 | 0.096 | 0.067 |
| NGC 5846 | 0.005717 | 58.5 | - | 0.52 | 21.0 ± 1^b | 0.57 ± 0.04 | 0.047 | - |
| NGC 5982 | 0.010064 | 4.5 | 1.9 | 0.90 | 0.5 ± 0.5^b | 1.23 ± 0.04 | 0.010 | 0.004 |
| NGC 6658 | 0.014243 | ≤ 3.0 | ≤ 0.3 | - | - | - | - | - |
| Previous work | | | | | | | | |
| NGC 193 ^f | 0.014723 | 5260 | 3184 | 0.53 | 1710 ± 102^g | 0.62 ± 0.04 | 34.217 | 20.710 |
| NGC 1587 ^f | 0.01230 | 655 | 222 | > 1.13 | 131 ± 5^b | 0.90 ± 0.04 | 2.042 | 0.692 |
| NGC 5044 ^h | 0.009280 | 229 | 38.0 | 1.88 | 35 ± 1^b | 1.05 ± 0.04 | 0.399 | 0.066 |
| NGC 5846 ^f | 0.005717 | - | 36.0 | - | - | - | - | 0.029 |
| NGC 7619 ^f | 0.012549 | 56.3 | 32.3 | 0.58 | 20 ± 1^b | 0.58 ± 0.04 | 0.195 | 0.112 |

^a Condon et al. (1998), ^b Brown et al. (2011), ^c Becker et al. (1995), ^d Kolokythas et al. (2015) ^e Kuhr et al. (1981), ^f Giacintucci et al. (2011), ^g Condon et al. (2002), ^h David et al. (2009)

in central galaxies consist of the normal double-lobed radio galaxies, small-scale jets, point sources and irregular-diffuse structures with no clear jet/lobe structure.

Our morphology classification is based on our dual-frequency GMRT analysis, the NVSS and FIRST data surveys and where needed, on the literature. Including the BGEs that are non-radio emitting at any frequency, we classify the radio emission seen from the BGEs in the following categories: i) *point-like* - unresolved radio point source, ii) *diffuse* emission - extended but amorphous with no preference in orientation, iii) *small-scale jets* - confined within the stellar body of the host galaxy, with extent < 20 kpc, and iv) *large-scale jets* - extending > 20 kpc, beyond the host galaxy and into the intra-group medium. In this class of radio sources we also include the subclass of *remnant jet* systems. These are systems which previous studies have shown to be the products of past periods of jet activity, and which are now passively ageing, without significant input from the AGN. Lastly, the systems that have no radio source detected are classed as category v) *absence of radio emission*. Table 3 lists the morphology of each source.

We note that some of our systems can be placed in more than one of the radio morphology classes described above. For example, the radio source in NGC 1167 appears as a *small-scale jet*

in our 610 MHz image, at 235 MHz the emission is *point-like*, but deeper 1.4 GHz observations have revealed the presence of a pair of old radio lobes extending > 100 kpc (Shulevski et al. 2012; Brienza et al. 2016). Since our interest is in the interaction between radio sources and their environment, in cases where the source can be placed in more than one category, we list the most extended class.

We find that 4 BGEs host large-scale jets (of which 2 are remnant jets), 2 host small-scale jets, 4 possess diffuse emission, while the remaining 14 radio-detected BGEs host point-like radio sources.

The two currently-active large-scale jet systems are NGC 193 and NGC 4261. Both are Fanaroff-Riley type I (FR I; Fanaroff & Riley 1974) radio galaxies (4C+03.01 and 3C 270 respectively) with their jet/lobe components extending several tens of kpc away from the host galaxy. The two sources present similar morphology with roughly symmetrical double-lobed structure and bright, straight jets. Of the remnant sources, NGC 1167 (4C+34.09) is also roughly symmetrical (Shulevski et al. 2012), while NGC 5044 has a single-sided bent jet and detached lobe.

Two BGEs, NGC 5153 and NGC 6658, lack radio emission in any of the frequencies we examined. A third galaxy, NGC 584,

is undetected in our GMRT data, but Brown et al. (2011) find a marginal detection of a faint point source at 1.4 GHz (0.6 ± 0.5 mJy). The noise levels of the GMRT observations (≤ 1 mJy at 610 and ≤ 6 mJy at 235 MHz; 5σ significance) are consistent with the non-detection of such a faint source.

5.2 Radio power in CLoGS BGEs

Using the measured radio flux densities, we calculated the radio power in each BGE for each frequency by:

$$P_\nu = 4\pi D^2(1+z)^{(\alpha-1)}S_\nu, \quad (1)$$

where D is the distance to the source, α is the spectral index, z the redshift and S_ν is the flux density of the source at frequency ν . In the case where no spectral index is known for the source (i.e., it is only detected at one frequency), α is by default set to 0.8 (Condon 1992), which is the typical value for extragalactic radio sources.

In figure 2, we show the radio power distribution of the BGEs in our sample at 235 and 610 MHz. The majority of the galaxies are having low powers in the range $10^{21} - 10^{23}$ W Hz⁻¹. Only one of our BGEs exhibits power in the range $10^{23} - 10^{24}$ W Hz⁻¹ (NGC 1587), but the sample contains three high-power sources with $P_{235\text{MHz}} > 10^{24}$ W Hz⁻¹. All three are bright jet hosting radio galaxies (NGC 4261, NGC 193 and NGC 5044). We note that typical relevant values of radio power at 235 and 610 MHz in BCGs ranges between $\sim 10^{23} - 5 \times 10^{26}$ W Hz⁻¹ (see e.g. Table 2, Yuan et al. 2016).

5.2.1 Radio-loudness in CLoGS BGEs

Only three of our BGEs can be considered radio-loud. We follow Best et al. (2005) in defining radio-loud systems as having $P_{1.4\text{GHz}} > 10^{23}$ W Hz⁻¹, and note that the NVSS and FIRST sensitivity limits mean that those of our systems which are undetected at 1.4 GHz must have radio powers below this limit. The three radio-loud systems are shown in Table 4.

Lin & Mohr (2007), using the same threshold of radio-loudness, found that while in high-mass clusters ($M_{200} > 10^{14.2} M_\odot$) $\sim 36\%$ of the BCGs have $P_{1.4\text{GHz}} > 10^{23}$ W Hz⁻¹, this fraction drops to only $\sim 13\%$ in low-mass clusters and groups ($10^{13} < M_{200} < 10^{14.2}$). The latter percentage is very similar to that observed in our sample, $\sim 12\%$ (3/26).

5.3 Contributions from star formation

While AGN are clearly the origin of the radio jet sources in our sample, we must consider whether star formation might contribute to the radio emission of the other sources, particularly those with low radio luminosities. We discuss the diffuse sources in detail in §6.5, but note here that their luminosity and morphology makes star formation unlikely to be their dominant source of radio emission. For the point-like sources, the beam sizes limit the emission to regions a few kiloparsecs across, but except in the most luminous systems, it is possible that we could mistake a compact central star forming region for AGN emission. Our CO survey of CLoGS BGEs confirms that the sample includes galaxies whose radio emission would be consistent with the star formation expected from their molecular gas reservoirs, if they were forming stars at rates similar to those in spiral galaxies (O’Sullivan et al., in prep.)

We will investigate star formation in these galaxies more thoroughly in a later paper (Kolokythas et al., in prep.), but for now we

need only determine whether it is likely to be a significant source of radio emission. To do this, we use Far-Ultraviolet (FUV) fluxes from the Galaxy Evolution Survey (Martin 2005) GR6 catalog³ to estimate the star formation rate (SFR) using the calibration from Salim et al. (2007). We then calculate the expected 610 MHz radio emission from star formation at that rate using the relation of Garn et al. (2009). A table of SFR and expected radio power for the BGEs with point-like and diffuse radio emission is provided in Appendix B. We find that in most cases, the detected radio emission is 1–2 orders of magnitude more luminous than would be expected from the FUV SFR. For three galaxies (NGC 924, NGC 2563 and NGC 5982) SF may contribute 20–40% of the radio emission, and in one (NGC 584) it may be the dominant source of radio emission. There is also one galaxy (NGC 4169) for which no FUV flux is available. We therefore consider that SF dominates at most 2 of the 14 BGEs with point-like emission, though it could have some impact on our measurements of radio properties in 1–3 more.

5.4 235 MHz radio power and largest linear size

Figure 3 shows the 235 MHz power of our sources plotted against their largest linear size (LLS) at any radio frequency, with data points from the study of Giacintucci et al. (2011) for comparison. For all resolved radio sources (i.e., excluding point-like sources) the largest linear size was measured across the maximum extent of the detected radio emission, at the frequency at which the emission is most extended. The resolved radio sources of the CLoGS central galaxies cover a large spatial scale from ~ 12 kpc (small scale jets; NGC 5846) to > 200 kpc (large scale jets; NGC 1167) with 235 MHz radio powers in the range $\sim 5 \times 10^{21}$ W Hz⁻¹ to $\sim 5 \times 10^{24}$ W Hz⁻¹.

Our CLoGS radio sources seem to follow the same linear correlation between size and power noted by Ledlow et al. (2002) and Giacintucci et al. (2011). Although the sample in Giacintucci et al. (2011) included only cavity systems in groups, and the work of Ledlow et al. (2002) included radio-sources that resided in rich clusters, we see that this linear correlation holds over 3 orders of magnitude at 235 MHz and extends to low power radio sources.

5.5 Spectral index

The spectral index of synchrotron emission corresponds to the index of the energy distribution of the relativistic electrons in the source which, in the absence of energy injection, will steepen over time owing to synchrotron and inverse Compton losses (e.g., de Zotti et al. 2010). In our sample, 19/26 galaxies are detected at both 610 and 235 MHz. Considering only these two frequencies, we find that 2/20 sources have a steep radio spectra with $\alpha_{235}^{610} > 1$ (NGC 1587 and NGC 5044) while the majority of the sources range from very flat values of $\alpha_{235}^{610} \sim 0.2$ to typical radio synchrotron spectra of $\alpha_{235}^{610} \sim 0.9$. Only NGC 940 presents a flux density greater at 610 MHz than in 235 MHz giving an inverted spectral index of $\alpha_{235}^{610} = -0.28 \pm 0.04$. Leaving the two steep spectrum outliers out, we find that the mean spectral index value for the 17/19 radio sources that reside in the central galaxies of our groups sample is $\alpha_{235}^{610} = 0.53 \pm 0.16$.

We can also measure the spectral index between 235 and 1400 MHz for 18/26 BGEs. The plots of the spectral distribution of the BGEs detected at both GMRT 235/610 MHz and 1.4 GHz

³ <http://galex.stsci.edu/GR6/?page=mastform>

Table 3. Morphological properties of CLoGS high-richness groups and their central radio sources. For each group we note the LGG number, the BGE name, the angular scale, the largest linear size (LLS) of the radio source, measured from the 235 MHz radio images unless stated otherwise, the radio and X-ray morphology class (X-ray class drawn from paper I), the energy output of any radio jets, estimated from 235 MHz power or from the X-ray cavities (P_{cav} ; see also paper I), and lastly the relevant cooling X-ray luminosity L_{cool} .

| Group | BGE | Scale (kpc'') | LLS (kpc) | Radio morphology | X-ray morphology | Energy output (radio) (10^{42} erg s $^{-1}$) | P_{cav} (10^{42} erg s $^{-1}$) | L_{cool} (10^{40} erg s $^{-1}$) |
|---------|------------|------------------|------------------|------------------|------------------|--|---|--|
| LGG 9 | NGC 193 | 0.359 | 80 ^a | large-scale jet | Group | 43.57 $^{+22.18}_{-14.70}$ | 4.66 $^{+3.55}_{-3.63}$ | 2.35 $^{+0.13}_{-0.08}$ |
| LGG 18 | NGC 410 | 0.373 | ≤ 11 | point | Group | - | - | - |
| LGG 27 | NGC 584 | 0.121 | $\leq 3^b$ | point | Galaxy | - | - | - |
| LGG 31 | NGC 677 | 0.378 | 30 | diffuse | Group | - | - | - |
| LGG 42 | NGC 777 | 0.354 | ≤ 8 | point | Group | - | - | - |
| LGG 58 | NGC 940 | 0.359 | ≤ 6 | point | Point | - | - | - |
| LGG 61 | NGC 924 | 0.310 | $\leq 4^c$ | point | Point | - | - | - |
| LGG 66 | NGC 978 | 0.334 | $\leq 3^c$ | point | Galaxy | - | - | - |
| LGG 72 | NGC 1060 | 0.368 | 14 | small-scale jet | Group | 1.13 $^{+0.16}_{-0.19}$ | 0.18 $^{+0.31}_{-0.03}$ | 45.70 $^{+1.40}_{-1.30}$ |
| LGG 80 | NGC 1167 | 0.349 | 240 ^d | remnant jet | Point | 34.68 $^{+15.84}_{-10.87}$ | - | - |
| LGG 103 | NGC 1453 | 0.305 | ≤ 11 | point | Group | - | - | - |
| LGG 117 | NGC 1587 | 0.252 | 22 ^a | diffuse | Group | - | - | - |
| LGG 158 | NGC 2563 | 0.315 | ≤ 3 | point | Group | - | - | - |
| LGG 185 | NGC 3078 | 0.165 | 26 | diffuse | Galaxy | - | - | - |
| LGG 262 | NGC 4008 | 0.262 | ≤ 7 | point | Galaxy | - | - | - |
| LGG 276 | NGC 4169 | 0.218 | $\leq 3^c$ | point | Point | - | - | - |
| LGG 278 | NGC 4261 | 0.155 | 80 | large-scale jet | Group | 64.32 $^{+38.79}_{-24.20}$ | 21.45 $^{+4.37}_{-3.04}$ | 8.00 $^{+0.40}_{-0.01}$ |
| LGG 310 | ESO 507-25 | 0.218 | 11 | diffuse | Galaxy | - | - | - |
| LGG 338 | NGC 5044 | 0.184 | 63 ^a | remnant jet | Group | 1.85 $^{+0.14}_{-0.15}$ | 2.00 $^{+1.74}_{-0.33}$ | 310.00 $^{+4.00}_{-9.00}$ |
| LGG 345 | NGC 5084 | 0.112 | ≤ 4 | point | Galaxy | - | - | - |
| LGG 351 | NGC 5153 | 0.291 | - | - | Galaxy | - | - | - |
| LGG 363 | NGC 5353 | 0.170 | ≤ 10 | point | Group | - | - | - |
| LGG 393 | NGC 5846 | 0.126 | 12 ^a | small-scale jet | Group | 0.41 $^{+0.11}_{-0.15}$ | 1.45 $^{+0.42}_{-0.38}$ | 34.50 $^{+0.70}_{-0.80}$ |
| LGG 402 | NGC 5982 | 0.213 | ≤ 3 | point | Group | - | - | - |
| LGG 412 | NGC 6658 | 0.305 | - | - | Point | - | - | - |
| LGG 473 | NGC 7619 | 0.262 | $\leq 6^a$ | point | Group | - | - | - |

^a Giacintucci et al. (2011), ^b Measured from the 1.4 GHz image, ^c Measured from the 610 MHz image, ^d Shulevski et al. (2012) (1.4 GHz)

Table 4. Radio-loud AGN ($P_{1.4\text{GHz}} > 10^{23}$ W Hz $^{-1}$) in CLoGS group dominant early-type galaxies. Columns show the LGG number, the BGE name and the 1.4 GHz power.

| Group | BGE | $P_{1.4\text{GHz}}$ (10^{23} W Hz $^{-1}$) |
|---------|----------|---|
| LGG 9 | NGC 193 | 11.1 \pm 0.6 |
| LGG 80 | NGC 1167 | 10.5 \pm 0.6 |
| LGG 278 | NGC 4261 | 23.2 \pm 0.5 |

from NVSS are shown in Appendix C, from which we see that in most cases a simple powerlaw provides a reasonable representation of the spectrum as a whole for each central galaxy. Only small deviations from a powerlaw are observed in some systems that can be attributed mainly to the small flux density offsets at specific frequencies either due to a difference in morphology between the two GMRT frequencies (e.g., NGC 5044, ESO 507-25, NGC 1060) or the lower sensitivity at 235 MHz. The mean value of α_{235}^{1400} calculated for the 18/26 BGEs with both 235 and 1400 MHz data, is 0.60 ± 0.16 .

In the case of the two steep spectra systems (NGC 1587 and NGC 5044), we observe a deviation from a simple powerlaw. This is caused by differences in morphology between frequencies, with both the remnant jet in NGC 5044 and the diffuse emission around

NGC 1587 being only visible at 235 MHz. The steep spectra of these sources is an indicator that we are observing radio emission from different outbursts (see also Giacintucci et al. 2011).

Table 5 shows the mean values of the spectral indices for each radio morphology class. Naturally, the steepest mean indices are found for the remnant jets. The mean indices for the other classes are all comparable within the uncertainties, although there is a hint that as expected, steeper spectra are found in diffuse sources and small jet systems, and flatter spectra in the point-like sources.

For the four sources where extended emission was observed at both 235 and 610 MHz we also calculated separate spectral indices for the core and the extended components by creating images with matched resolution. Table 6 lists these spectral index values. In three systems (NGC 193, NGC 677, NGC 3078) we find that the spectral index does not differ between the two components. Only NGC 4261 exhibits a flatter core index, probably as a result of the ‘cosmic conspiracy’ (see Cotton et al. 1980), or the presence of free-free emission (see Kolokythas et al. 2015, for a more in-depth discussion).

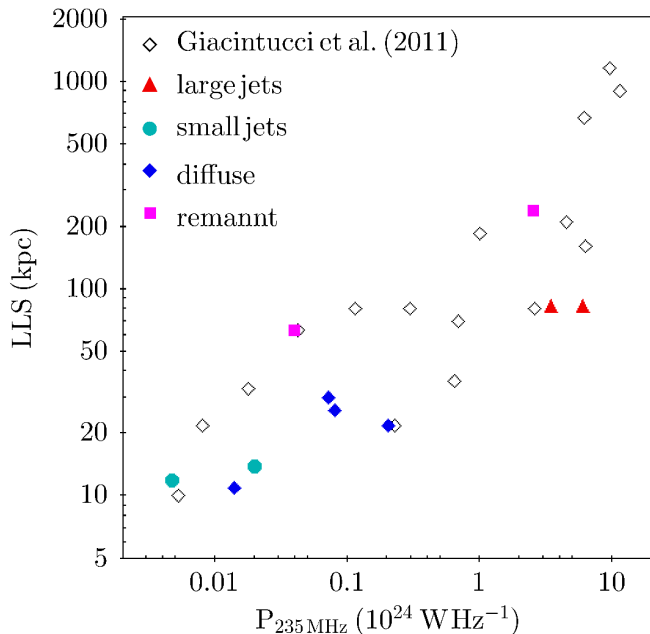


Figure 3. Radio power at 235 MHz plotted against the largest linear size of radio sources associated with the central brightest group ellipticals of the CLoGS high-richness sample, with data points from Giacintucci et al. (2011) for comparison. Different symbols indicate the radio morphology of the CLoGS sources.

Table 5. Mean spectral indices α_{235}^{610} and α_{235}^{1400} for the different radio morphologies of our sources.

| Radio Morphology | Mean α_{235}^{610} | Mean α_{235}^{1400} |
|------------------|---------------------------|----------------------------|
| Point-like | 0.46 ± 0.11 | 0.54 ± 0.11 |
| Small-scale jet | 0.70 ± 0.06 | 0.60 ± 0.06 |
| Remnant jet | 1.24 ± 0.06 | 0.77 ± 0.06 |
| Large-scale jet | 0.53 ± 0.06 | 0.57 ± 0.06 |
| Diffuse emission | 0.64 ± 0.07 | 0.65 ± 0.09 |

6 DISCUSSION

6.1 Detection statistics and comparisons

The comparison between group and cluster samples in radio requires caution, since the most relevant studies have not used exactly the same selection criteria (eg. distance, radio power etc). Several studies have investigated the radio detection fraction of brightest cluster galaxies, group-dominant galaxies and large ellipticals in the local Universe. Dunn et al. (2010), using a sample of nearby

Table 6. 235-610 MHz spectral indices for the cores and extended emission of those radio sources in our sample with their morphology resolved at both GMRT frequencies. Columns show the LGG number, the BGE name, the radio morphology and the spectral index α_{235}^{610} of the core and the surrounding emission of each source.

| Group | BGE | Core α_{235}^{610} | Surrounding α_{235}^{610} |
|---------|----------|---------------------------|----------------------------------|
| LGG 9 | NGC 193 | 0.54 ± 0.04 | 0.53 ± 0.04 |
| LGG 31 | NGC 677 | 0.79 ± 0.04 | 0.82 ± 0.04 |
| LGG 185 | NGC 3078 | 0.43 ± 0.04 | 0.45 ± 0.04 |
| LGG 278 | NGC 4261 | 0.20 ± 0.04 | 0.52 ± 0.04 |

bright ellipticals, most of which reside in galaxy groups or clusters, found that $\sim 81\%$ (34/42) are detected using the NVSS and Sydney University Molonglo Sky Survey (SUMSS, 843 MHz), rising to $\sim 94\%$ (17/18) for those systems with *ROSAT* All-Sky Survey 0.1–2.4 keV X-ray fluxes $> 3 \times 10^{-12} \text{ erg s}^{-1} \text{ cm}^{-2}$ (equivalent to $L_{0.1-2.4\text{keV}} \sim 2.3 \times 10^{42} \text{ erg s}^{-1}$ at the distance limit of CLoGS). For comparison with CLoGS we detect 21/26 BGEs from NVSS ($\sim 81\%$) whereas all of our groups above the equivalent X-ray flux limit from Dunn et al. (2010) sample are detected (5/5; 100%). Using the X-ray selected groups sample of Eckmiller et al. (2011), Bharadwaj et al. (2014) found that 20/26 BGEs (77%), are detected in radio using the NVSS, SUMSS and VLA Low frequency Sky Survey (VLSS, 74 MHz) radio catalogs. In the X-ray selected local, low mass cluster sample of Magliocchetti & Brüggén (2007), the radio detection rate in central BCGs is 20% when using a radio luminosity limit of $L_{1.4\text{GHz}} > 10^{22} \text{ W Hz}^{-1}$ (our detection rate with CLoGS above this limit is 7/26, $\sim 27\%$), rising to 92% (11/12 of BCGs) when this limit is lowered to $L_{1.4\text{GHz}} > 10^{20} \text{ W Hz}^{-1}$, comparable to the sensitivity of our sample. These results agree with our own in suggesting that, with sufficiently deep observations, almost all group or cluster dominant galaxies will be found to host a central radio source.

Comparison with more massive clusters is difficult, since they tend to be much more distant than our groups, with radio surveys usually identifying only the brightest central radio sources. We note that numerous earlier X-ray selected cluster samples suggest a radio detection rate for BCGs $\sim 50\%$ (e.g., B55 sample Edge et al. 1990; Peres et al. 1998, Highest X-ray Flux Galaxy Cluster Sample, HIFLUGCS Reiprich & Böhringer 2002; Mittal et al. 2009), for sources of sufficient power to be detected in volumes extending out to $z = 0.3$. A similar radio detection rate for BCGs was also found by Ma et al. (2013) in a combined sample of X-ray selected galaxy clusters matched with NVSS ($\sim 52\%$ for radio sources $> 3 \text{ mJy}$) and Kale et al. (2015) ($\sim 48\%$; matched with NVSS and FIRST catalogs) in a combined sample of 59 X-ray selected BCGs extracted from the Extended Giant Metrewave Radio Telescope (GMRT) Radio Halo Survey (EGRHS; Venturi et al. 2007, 2008). However, Lin & Mohr (2007) using a cluster sample from two large X-ray cluster catalogs drawn from the *ROSAT* All-Sky Survey (RASS), NORAS (Böhringer et al. 2000) and REFLEX (Böhringer et al. 2004), detected 122 BCGs in 342 clusters (36%) that have a radio component with flux density greater than 10 mJy at 1.4 GHz. The selection criterion of a cut-off at 10 mJy for the NVSS catalog matching is most probably the reason for this lower radio detection rate.

Another recent study by Hogan et al. (2015) using a combination of X-ray selected BCG samples matching with NVSS, SUMSS and FIRST radio catalogs finds a detection rate of $61.1 \pm 5.5\%$ for the extended Brightest Cluster Sample (eBCS; Ebeling et al. 2000), $62.6 \pm 5.5\%$ for the REFLEX-NVSS sample (ROSATESO Flux Limited X-ray; Böhringer et al. 2004) and $60.3 \pm 7.7\%$ for the REFLEX-SUMSS sample. These detection percentages are slightly higher compared to previous radio-BCG detection rates found in X-ray selected clusters, but are in good agreement within errors.

Comparing by visual inspection the maxBCG sample with FIRST, Huang & Chen (2010) identify 552 double-lobed central radio galaxies in the ~ 13000 cataloged clusters ($\sim 4\%$). In our sample, only NGC 193 and NGC 4261 are large and bright enough to be comparable, though NGC 1167 probably was, and NGC 5044 may have been, in the recent past. Within the large uncertainties, this suggests a comparable fraction of large, double-lobed sources be-

Table 7. Fraction of radio sources with a given radio morphology detected in X-ray bright and X-ray faint CLoGS high-richness groups.

| Radio Morphology | X-ray Bright | X-ray Faint |
|-----------------------|--------------|-------------|
| Point-like | 7/14 | 7/12 |
| Small/Large scale jet | 5/14 | 1/12 |
| Diffuse emission | 2/14 | 2/12 |
| No detection | 0 | 2/12 |

tween groups and clusters, though clearly larger samples of groups are needed for a more accurate comparison.

6.2 The X-ray environment of CLoGS central radio galaxies

While in cluster environments an X-ray emitting intra-cluster medium is almost always present (e.g., 72%; Balogh et al. 2011, 89%; Andreon & Moretti 2011) in our optically-selected groups sample we find that only $\sim 55\%$ of systems exhibit extended X-ray emission with luminosities and temperatures typical of group-scale haloes (see Paper I). In these X-ray bright groups, a variety of radio morphologies is observed, including group-group mergers (NGC 1060 and NGC 7619) and two recently tidally-disturbed ‘sloshing’ systems (NGC 5846 and NGC 5044, Gastaldello et al. 2013). In other cases, disturbances in the X-ray-emitting gas are caused by a central radio source (e.g., NGC 193). The radio jets seen in these systems can potentially heat the IGM (through a variety of mechanisms, see e.g., Fabian 2012), balancing radiative energy losses and helping to maintain the long-term thermal equilibrium of the IGM.

In examining interactions between the central radio galaxy and the IGM, we divided our groups into X-ray bright and X-ray faint subsets; X-ray bright groups are those which in Paper I we find to have group-scale haloes (extending > 65 kpc with $L_{X,R500} > 10^{41}$ erg s^{-1}), while X-ray faint groups are those that either have galaxy-scale diffuse or point-like X-ray emission. Using this classification, 14/26 of our groups are X-ray bright. Table 3 lists the radio and X-ray morphology of the central BGEs in the high-richness sub-sample.

Table 7 shows the fraction of X-ray bright and faint groups which host each class of central radio source. There is a clear environmental difference for the jet radio sources between X-ray bright and faint groups. All but one of the jet sources are found in X-ray bright systems, confirming that the X-ray bright groups or clusters are the preferred environment for radio jets (as found by, e.g., Magliocchetti & Brügggen 2007; McNamara & Nulsen 2007), even down to the relatively low mass range covered by our sample. This suggests that the presence of a group scale IGM provides a richer gas supply which is more likely to fuel an outburst by the central AGN. On the other hand, all galaxies that lack radio emission are found in X-ray faint systems. With only two non-detections, this is not a statistically significant result, but it hints at an environmental trend worth further investigation with larger samples. These X-ray faint groups may have shallow gravitational potentials that are unable to heat the available gas to temperatures where X-ray emission becomes detectable, (though this is perhaps unlikely given the sensitivity of our X-ray data and the velocity dispersions of the groups), or they may be deficient in diffuse intra-group gas and hence not bright enough, as has been suggested for other X-ray faint optically-selected groups (e.g., Rasmussen et al. 2006).

All radio jet systems in X-ray bright groups (5/5) reside in

cool cores (in agreement with the study of Sun 2009), suggesting that a cool core is a necessary requirement for jet activity in such systems. NGC 1167, the only jet source identified in an X-ray faint group, has an extensive cold gas reservoir, which has likely fueled the AGN outburst. Of the five X-ray bright jet-hosting systems, four show clear correlations between the GMRT low-frequency radio and X-ray structures, in the form of cavities and/or rims of enhanced X-ray emission surrounding the radio lobes. This provides proof of interactions between the central radio galaxy and the IGM. Of these four systems, the two large-scale, currently active radio jet systems (NGC 193 and NGC 4261) have large cavities or cocoon-like structures excavated and filled by the radio lobes. NGC 5846 and NGC 5044 possess smaller-scale cavities commensurate with their current radio activity, but there is evidence of a larger cavity correlated with the old, detached radio lobe of NGC 5044, from abundance mapping (O’Sullivan et al. 2014). In the fifth system, NGC 1060, the jets are too small for cavities to be resolved in the *XMM-Newton* observation described in Paper I.

However, the predominant radio morphology across all our groups is the point-like, found in $\sim 50\%$ of X-ray bright and $\sim 58\%$ of X-ray faint groups. In X-ray bright systems, point-like radio sources are common in both cool-core and non-cool core groups. Considering an AGN as the dominant source of radio activity (as most likely is the case in almost all of our point-like systems; see §5.3), this reveals that not only the environment, but also the efficiency of the processes involved plays a significant role in the morphology of a radio source. While in X-ray faint groups the lack of a significant quantity of gas to fuel the central engine may explain the presence of only low-power activity, in X-ray bright cool-core systems we must either invoke inefficiencies in fueling, or duty cycle effects (e.g., the need to build up a reservoir of cold, dense gas via cooling from the IGM after a previous round of feedback heating) to explain the lack of ongoing jet activity. Another possible explanation for low power point-like radio sources in both environments is a contribution from the stellar population.

We also note that diffuse radio sources appear equally common in both X-ray bright and X-ray faint groups. We discuss these sources further in § 6.5.

6.3 Environment and spectral index

In dense environments, such as the centres of galaxy clusters, it is known that radio galaxies usually present a steep synchrotron spectral slope compared to galaxies that reside in the field (e.g., Govoni et al. 2001; Bornancini et al. 2010). As the radio morphology of a galaxy depends on the environment in which it is embedded, we examine the radio spectral index distribution of the central galaxies in our sample in order to unveil any relation that may exist between spectral index and environment, comparing also with what is known for BCGs.

The typical range of spectral index values α , of radio galaxies at the centers of cool-core clusters is $1 - 2$ (Giacintucci et al. 2011). The simplest interpretation for such steep radio spectra is the restriction of the relativistic radio plasma in the central regions of the cluster by the high pressure and dense external medium, which may slow the expansion and consequent fading of the radio source (e.g., Fanti et al. 1995; Murgia et al. 1999). Giacintucci et al. (2011) observed 15 X-ray bright galaxy groups hosting extended radio sources with the GMRT at 235 and 610 MHz, and found that 9/15 had a steep spectral index of $\alpha_{235}^{610} > 1$. This is the opposite of what we find from our CLoGS sample, where only 2/26 BGEs host a steep-spectrum radio source. Clearly our inclusion of X-ray faint

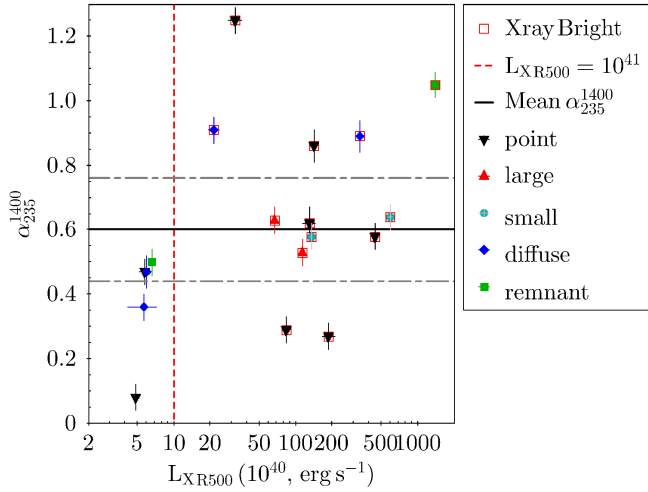


Figure 4. Spectral index distribution α_{235}^{1400} of BGEs compared to the group X-ray luminosity within R_{500} . The solid horizontal line indicates the average spectral index value of 0.60 at this frequency range, with the associated error bars shown as dot-dashed lines. The red dashed vertical line shows the threshold in X-ray luminosity ($L_{X R_{500}} = 10^{41}$ erg s $^{-1}$) above which we consider groups as X-ray bright.

groups and point-like central radio sources, some of which also have contribution from star-formation in their radio emission, has a significant impact on the spectral index distribution.

Our sources are more comparable to those found in the general population of galaxy clusters, both cool-core and non-cool-core. Bornancini et al. (2010), using a sample of maxBCG clusters, calculated the mean value of the spectral index for BCGs between 325 MHz and 1.4 GHz to be $\alpha_{325}^{1400} = 0.65$. This is similar to our mean spectral index ($\alpha_{235}^{1400} = 0.60 \pm 0.16$) using almost the same frequency range. The mean spectral index in cool-core groups alone is calculated to be $\alpha_{235}^{1400} = 0.72 \pm 0.13$, with the equivalent mean value in the non-cool-core ones being $\alpha_{235}^{1400} = 0.60 \pm 0.16$. We find that cool-core groups present steeper mean spectral index but taking into account the uncertainties in the values, the difference does not seem to be so strong.

Figure 4 shows spectral index α_{235}^{1400} plotted against $L_{X R_{500}}$, the X-ray luminosity of the group within the fiducial radius R_{500} . We find that radio sources with spectral indices steeper than the average value of $\alpha_{235}^{1400} = 0.60$ reside in X-ray bright groups, regardless of their radio morphology. These steeper-than-average sources include not only jets and known remnants of past outbursts, but also systems with point-like or diffuse radio morphology. This supports the interpretation suggested above, that radio sources remain visible for longer periods in environments with a dense IGM, while those in X-ray faint systems expand and fade relatively rapidly.

6.4 Radio emission and group spiral fraction

The environment in which a galaxy resides is known to play an important role on its properties. In galaxy groups, the fraction of early-type galaxies ranges from $\sim 25\%$ (as in the field) to $\sim 55\%$ (as in rich clusters, Mulchaey & Zabludoff 1998). A high fraction of spiral galaxies can be an indicator of a group’s dynamical youth. Systems whose collapse and virialisation occurred further in the past are expected to have higher fractions of early-type galaxies, since there has been a longer history of interactions and mergers. Studies in a sample of compact groups have suggested a correla-

tion between extended X-ray emission and low spiral fraction (e.g., Pildis et al. 1995) suggesting that dynamical age is linked to the ability to build and retain a hot IGM. We therefore explore whether any correlation between the close environment of a BGE and its radio morphology or the group’s X-ray emission exists, by looking at the spiral galaxy content of the member galaxies in our groups.

Table 8 shows the spiral fractions in each group. We took galaxy morphologies from HyperLEDA⁴, classifying them as either early-type (morphological T-type < 0), late-type (T-type ≥ 0) or unknown. As the objects with unknown morphology are typically faint and small, we consider them as dwarf galaxies and include them with the late-type galaxies, defining spiral fraction F_{sp} as the number of late-type or unknown morphology galaxies over the total number of group members.

We follow Bitsakis et al. (2010) in considering groups with $F_{sp} > 0.75$ as spiral-rich, and potentially dynamically young. We find that 11/26 (42%) of our groups are classified as spiral-rich and 15/26 (58%) as spiral-poor. Bitsakis et al. (2014), considering a sample of 28 Hickson compact groups (HCGs, Hickson 1992) which are likely to have a higher rate of galaxy interaction than most of our groups (Hickson 1997), finds a similar fraction to our sample with 46% (13/28) being spiral-rich and 54% (15/28) being spiral-poor.

Fig 5 shows the relation between F_{sp} and the X-ray luminosity calculated at R_{500} , $L_{X R_{500}}$. Point-like radio sources appear to be equally divided between dynamically young and old groups therefore showing no preference in the group environment they reside. We further find that in high spiral fraction groups the radio point-like systems are almost evenly distributed between X-ray bright (3/7) and X-ray faint groups (4/7). In Ponman et al. (1996) a mild trend between spiral fraction systems and diffuse X-ray luminosity is suggested using ROSAT observations over a sample of HCGs. In our sample however, we see that spiral-rich systems have no particular preference in the X-ray environment, since 6/11 spiral-rich groups are X-ray faint and 5/11 X-ray bright.

For fig 5 a Spearman correlation coefficient $\rho = -0.17$ with $P = 0.42$ is found, showing that the association between F_{sp} and $L_{X R_{500}}$ for our groups cannot be considered statistically significant. However, we point out that the majority of spiral-rich systems with $L_{X R_{500}} < 10^{42}$ erg s $^{-1}$, 75% (6/8), appear to exhibit point-like radio emission and that 67% (4/6) of the jet systems resides in dynamically old groups.

Fig 6 shows the relation between F_{sp} and the radio power at 235 MHz ($P_{235 MHz}$) for the systems with radio emission detected at 235 MHz. We find that the majority of radio point-like systems (6/9) detected at 235 MHz resides in groups with higher spiral fractions (dynamically young) with a mean spiral fraction of 0.73 ± 0.12 . Comparing with the mean value for jet sources (0.66 ± 0.21) we find that point radio sources have a marginally higher mean F_{sp} but, given the large errors this result cannot be regarded as statistically significant.

While the suggestion that BGEs with point-like radio emission may be more common in X-ray faint, dynamically young groups is interesting, the lack of a clear trend is perhaps more telling. Point-like emission might be expected from the low accretion rates of AGN in hot-gas-poor systems, and in some cases star formation fueled by cold gas (perhaps more common in X-ray faint groups) may make a contribution, but low radio luminosities and point-like emission would also be expected in the interludes between outbursts of

⁴ <http://leda.univ-lyon1.fr/>

Table 8. Spiral fraction for the high-richness sub-sample CLoGS groups. We note the brightest group early-type galaxy and the spiral fraction F_{sp} , which is the ratio of the number of late-type plus unknown galaxies over the total number of galaxies.

| BGE | Spiral fraction F_{sp} |
|------------|-----------------------------|
| NGC 193 | 0.67 |
| NGC 410 | 0.52 |
| NGC 584 | 0.64 |
| NGC 677 | 0.91 |
| NGC 777 | 0.56 |
| NGC 940 | 0.78 |
| NGC 924 | 0.71 |
| NGC 978 | 0.60 |
| NGC 1060 | 0.80 |
| NGC 1167 | 0.75 |
| NGC 1453 | 0.76 |
| NGC 1587 | 0.62 |
| NGC 2563 | 0.72 |
| NGC 3078 | 0.74 |
| NGC 4008 | 0.88 |
| NGC 4169 | 0.88 |
| NGC 4261 | 0.71 |
| ESO 507-25 | 0.57 |
| NGC 5044 | 0.53 |
| NGC 5084 | 0.82 |
| NGC 5153 | 0.79 |
| NGC 5353 | 0.91 |
| NGC 5846 | 0.48 |
| NGC 5982 | 0.86 |
| NGC 6658 | 0.60 |
| NGC 7619 | 0.62 |

jet activity in BGEs at the centres of cooling flows (group relevant timescales $\sim 10^7 - 10^8$ yr; see David et al. 2011, Machacek et al. 2011, Randall et al. 2011, Rafferty et al. 2013). The presence of jets in dynamically young systems also indicates the diverse factors which can affect nuclear activity, with our sample including at least one example of powerful remnant jets likely fueled by interactions with a cold gas rich neighbor.

6.5 Diffuse radio sources in group central galaxies

The origin of the diffuse radio sources that we find in our groups is somewhat mysterious. They have some similarities to the radio mini-halos seen in cool core clusters (e.g., Mazzotta & Giacintucci 2008; Doria et al. 2012; Kale et al. 2013). The scale of the diffuse emission in our groups is small, only a few tens of kpc, whereas mini-halos in clusters can extend up to a few hundreds of kpc in radius. Turbulence in groups is considerably weaker than in clusters, and is generally thought not to be capable of providing the energy necessary to accelerate the electron population and produce radio emission. It is also notable that the groups in which we see evidence of mergers and tidal disturbances do not host diffuse radio sources. It therefore seems unlikely that our sources are radio halos or mini-halos.

Of our four diffuse radio sources, in three cases the diffuse emission is only observed at 610 MHz. This is a result of the significantly superior sensitivity achieved at 610 MHz, 5 – 30 times better than that at 235 MHz in these systems. We find no clear correlation between X-ray and radio structure for the diffuse sources; only two of the four reside in X-ray bright groups, and in those two

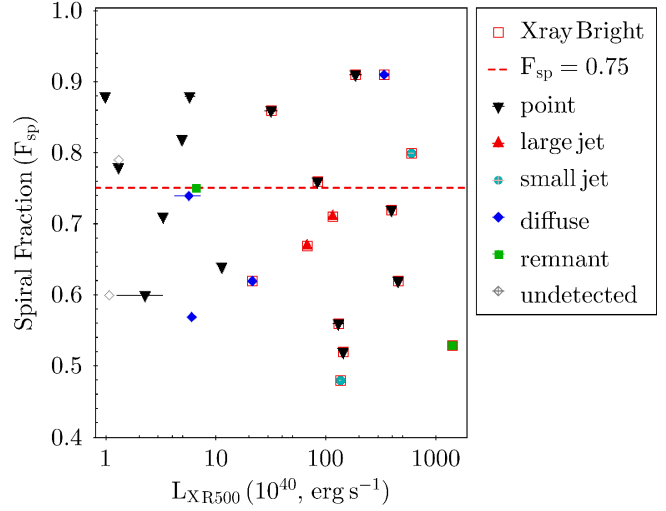


Figure 5. Spiral fraction F_{sp} , i.e. the number of late type+unknown galaxies over the total number of galaxies in each group, of different radio morphologies in relation to the X-ray luminosity at R_{500} ($L_{X R_{500}}$). The X-ray bright groups are marked in red square, different radio morphologies are shown in different symbols, whereas the red line indicates a spiral fraction of 0.75 following Bitsakis et al. (2010).

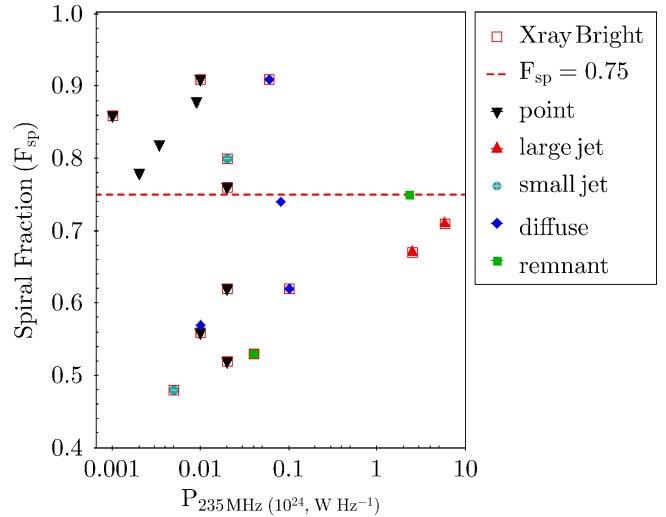


Figure 6. Spiral fraction F_{sp} as in fig. 5, in relation to radio power at 235 MHz ($P_{235 MHz}$). The radio morphology of each group can also be seen here in different symbols, with the X-ray bright groups being marked in red square.

(NGC 677 and NGC 1587) no cavities or shock fronts are observed. The spectral indices of these two sources are relatively steep, and the radio emission is more extended than the stellar population of the galaxies, ruling out star formation as the dominant source of emission.

The spectral indices of the two diffuse sources in X-ray faint groups are relatively flat. They are therefore unlikely to be radio phoenixes or relic radio galaxies. Of the two X-ray faint systems, NGC 3078 presents the more interesting morphology. Located in a galaxy-scale X-ray halo, at both 235 and 610 MHz it shows a clear, relatively symmetric east-west extension, roughly matching the minor axis of its host galaxy and confined within the stellar body of the galaxy (at least in projection). This morphology could indicate

a galactic wind or an outflow associated with a failed or decollimated jet source. A second possibility is star-formation. However, using the relation of Garn et al. (2009) we find the expected star-formation rate only from the diffuse 610 MHz emission (excluding the central point source) to be $\sim 2.5 M_{\odot} \text{ yr}^{-1}$, which is an order of magnitude higher than the rate expected from mid-infrared *Wide-field Infrared Survey Explorer (WISE)* W3 luminosity ($\sim 0.2 M_{\odot} \text{ yr}^{-1}$). ESO 507-25, located in another galaxy-scale X-ray halo, is less structured, with diffuse emission extending in all directions, again on scales smaller than the stellar extent. As in NGC 3078, star formation can be ruled out as the main origin of the radio emission in this system, as the predicted rate ($\sim 1.20 M_{\odot} \text{ yr}^{-1}$) is again almost an order of magnitude greater than what would be consistent with the WISE L_{W3} rate ($\sim 0.17 M_{\odot} \text{ yr}^{-1}$). In addition, for both of these systems the SFR_{FUV} rates are also too low (see Appendix B). The flat spectral indices of these sources ($\alpha_{235}^{1400} = 0.35 \pm 0.14$ and 0.47 ± 0.05) suggest ongoing activity. In general, it seems that while star formation may make a contribution to some of our diffuse radio sources, it cannot be the dominant source of emission in any of them.

We are left to conclude that there is no clear single origin for these sources, and that we may be observing sources with a similar appearance but different formation mechanisms, depending on their environments. A group-scale IGM can plausibly confine old radio lobes in the group core and, over time, IGM gas motions may alter their morphology until the lobe structure is lost. In NGC 1587, an ongoing encounter with a companion galaxy, NGC 1588, could raise the possibility of shock-driven re-acceleration, but the lack of a clear correlation between the radio and X-ray morphologies (i.e., no clear shock fronts or correlated surface brightness edges) is a problem for this hypothesis. In the X-ray faint groups, the flat spectral indices make relic radio lobes an unlikely explanation, but a disrupted jet may provide an explanation for the emission in NGC 3078.

6.6 Power output of jet systems

For the BGEs that host jet sources, we estimate the mechanical power output of the jets using an approach similar to that described in O’Sullivan et al. (2011). For NGC 193, NGC 4261, and NGC 5044 and NGC 5846 cavity size was estimated from the X-ray images. For NGC 1060, the spatial resolution of the available *XMM-Newton* data were insufficient to resolve cavities on the scale of the small-scale jet seen only at 610 MHz. We therefore estimated the cavity size from the 610 MHz extent. We defined the mechanical power output estimated from the cavities P_{cav} as:

$$P_{\text{cav}} = \frac{4p_{th}V}{t_{\text{cav}}}, \quad (2)$$

where p_{th} is the value of the azimuthally-averaged pressure profile at the radius of the cavity centre, V is the cavity volume, and t_{cav} is an estimate of the age of the cavity. We chose to use the sonic timescale (i.e., the time required for the cavity to rise to its current position at the local sound speed in the IGM) so as to facilitate comparison with estimates from the literature. The sonic timescale was calculated by

$$t_{\text{cav}} = \frac{r_{\text{cav}}}{\sqrt{\frac{\gamma kT}{m}}}, \quad (3)$$

where r_{cav} is the mean radius of the cavity from the nucleus, γ is the adiabatic index of the IGM (taken to be $5/3$), k is Boltzmann’s constant, T is the IGM temperature, and m is the mean particle

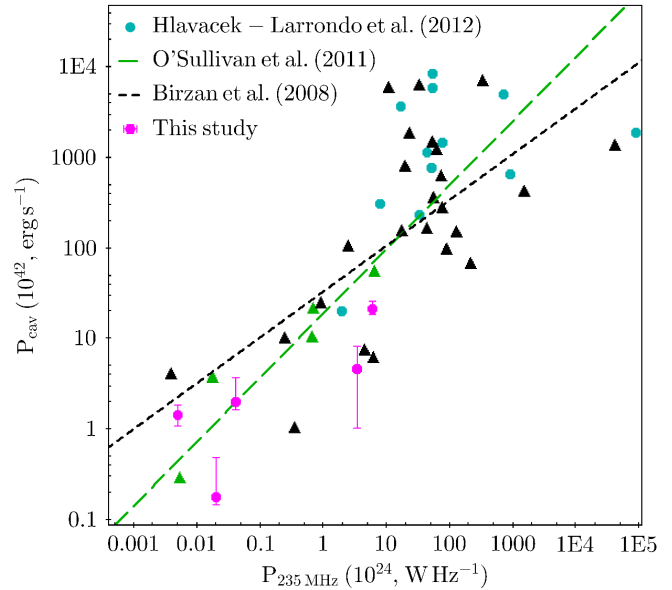


Figure 7. Cavity power P_{cav} calculated from X-rays vs. radio power at 235 MHz. Systems of our groups sample are marked by pink circles with errors, members from Hlavacek-Larrondo et al. (2012) are shown by cyan circles, members from O’Sullivan et al. (2011) are in green triangles and members from Birzan et al. (2008) in black triangles. Note that for the three systems in common between CLoGS and O’Sullivan et al. (2011) (NGC 193, NGC 5044 and NGC 5846) we use the CLoGS measurements. The black dotted line indicates the relation found by Birzan et al., and the green dashed that of O’Sullivan et al.

mass in the IGM. We also note that for NGC 5044, we exclude the detached radio lobe from consideration, since its filling factor and age cannot be accurately estimated, and only include the cavities identified in David et al. (2017). Our estimates of P_{cav} are listed in Table 3. We find mechanical power values in the range $\sim 10^{41} - 10^{43} \text{ erg s}^{-1}$, typical for galaxy groups.

Fig. 7 shows the relation between the mechanical power output (P_{cav}) and the radio power at 235 MHz (P_{235}) for the 5 jet systems in the CLoGS high-richness sub-sample. Our galaxy groups fall in the lower end of the range covered by the 24 groups and clusters described by Birzan et al. (2008) and are in good agreement with the 7 groups of O’Sullivan et al. (2011). This is unsurprising given the overlap between the samples (three systems in common; NGC 193, NGC 5044 and NGC 5846). NGC 1060 has one of the lowest observed cavity powers, suggesting that either the cavities are larger than the 610 MHz emission, or that its small lobes are still young and are as yet over-pressured with respect to the IGM.

One goal of measuring the relationship between radio power and cavity power is to allow estimates of feedback in systems where high-quality X-ray data are not available. The surveys performed by the eROSITA mission are expected to detect tens of thousands of groups and poor clusters (Merloni et al. 2012; Pillepich et al. 2012), but are unlikely to provide reliable estimates of cavity size. The use of radio data as a proxy estimator of AGN power output will therefore be important when studying this population.

We can consider the likely effectiveness of such an approach by applying it to our data, using the $P_{\text{cav}} - P_{235}$ relation measured by O’Sullivan et al. (2011) to estimate a cavity power based on the radio power. The 235 MHz radio power is used since low frequencies are least likely to be affected by spectral aging. One immediate benefit is that we can estimate a mechanical power output for

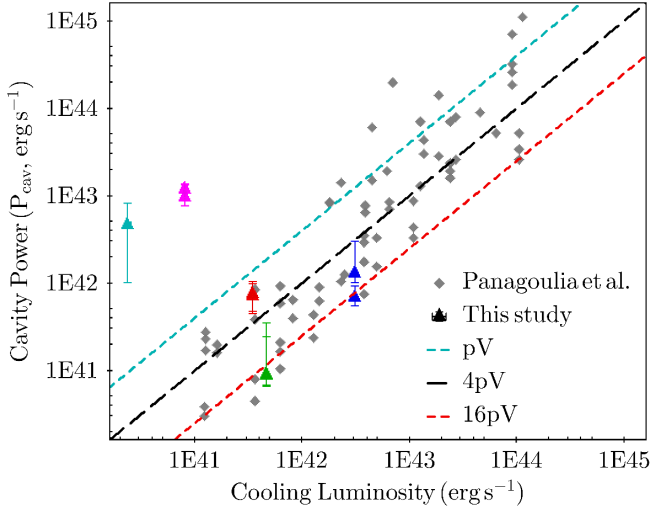


Figure 8. Cavity power from the X-rays in relation to the cooling luminosity, L_{cool} , calculated in the 0.5–7 keV band for our CLoGS groups (colored triangles; see Table 4) in comparison to the groups and clusters used in the sample study of Panagoulia et al. (2014)). In order from left to right for the data from this study, cyan and pink triangles represent the large-scale jet systems (NGC 193 and NGC 4261), whereas red, green and blue triangles represent the small-scale jet ones (NGC 5846, NGC 5044 and NGC 1060).

NGC 1167, where no X-ray luminous IGM is detected. As expected for such an extended source, the old radio lobes of NGC 1167 imply that during the period of activity, the jets in this systems had a large mechanical power output, $\sim 3.5 \times 10^{43} \text{ erg s}^{-1}$.

Table 3 lists the radio-estimated jet powers for the six groups. We find that these estimates are in agreement with the X-ray estimate of P_{cav} for NGC 5044, but disagree for the small-scale jet sources and the large-scale jet systems with high P_{235MHz} . For the small jets, we find both under- and over-estimates, probably arising from the relatively large scatter in the relation. We note that this scatter appears to be a product on the intrinsic uncertainties in cavity measurements, and is not significantly improved at other frequencies (see, e.g., Birzan et al. 2008; Kokotanekov et al. 2017).

For the large scale jets, the radio estimate of cavity power is greater than the X-ray measurement, though the large uncertainties on the radio estimate make the differences only $\sim 2\sigma$ significant. Both NGC 4261 and NGC 193 have shells of X-ray emission surrounding their radio lobes, indicating that the lobes are still over-pressured and expanding trans-sonically. It is therefore possible that for these systems the X-ray cavity power is actually an underestimate of the true jet power. We might expect the radio and X-ray estimates to come into agreement as these sources age, expand, and reach equilibrium with the surrounding IGM.

6.6.1 Heating vs Cooling

We can also examine the balance between heating by the central AGN source and radiative cooling of the IGM core. Fig. 8, shows the ratio P_{cav} compared with the cooling luminosity L_{cool} (see § 3.2), over-plotted on data from the sample of Panagoulia et al. (2014).

Comparing our results to Panagoulia et al. (2014) we find that the small-scale jet systems NGC 1060 and NGC 5846, along with the remnant jet in NGC 5044, lie within the scatter about the relation, indicating approximate thermal balance. The large-scale jet

systems NGC 193 and NGC 4261 fall about two orders of magnitude above the relation, suggesting that they are significantly over-powered. It is notable that in both systems the size of the jets and lobes greatly exceeds that of the cooling region. NGC 4261 has a small cool core, only ~ 10 kpc in radius (O’Sullivan et al. 2011) which corresponds to the cooling region as defined here. Its jets extend ~ 40 kpc on each side (see also Kolokythas et al. 2015 for a detailed radio study), and seem to primarily impact the surrounding IGM, having excavated wedge-shaped channels to exit the core. The radio lobes of NGC 193 seem to have formed a cocoon or series of cavities with compressed gas rims, leaving little cool gas in the galaxy core. We note that the exceptional power of the outburst is not dependent on our assumption of a single cavity; using the jet powers estimated by Bogdan et al. (2014) for a pair of cavities produces similar results. This may indicate that in both systems, cooling and heating have become detached, with the jets heating the IGM without significantly impacting the material which is fueling the AGN. In this case, absent some disturbance, we would expect these outbursts to continue until they exhaust the ability of the cool core to provide fuel.

6.7 AGN feedback in CLoGS groups

Previous observational studies have suggested that feedback in most galaxy groups and clusters operates in a near-continuous ‘bubbling’ mode (e.g., Birzan et al. 2008, 2012; Panagoulia et al. 2014), in which feedback heating is relatively gentle. This model has been supported by theoretical studies (e.g., Gaspari et al. 2011). Our small-scale and remnant jet systems seem to fit in with this picture. However, there are counter-examples. Nulsen et al. (2007, 2009) found that the cavity power of a number of giant ellipticals (some of which are the dominant galaxies of groups and clusters) exceeds their cooling luminosity by up to an order of magnitude. Rafferty et al. (2006) give the example of the exceptionally powerful outburst in the cluster MS 0735+7421, which again greatly exceeds the cooling luminosity, even though using a longer cooling time threshold and consider bolometric X-ray luminosity. Investigating the effect of heating in the same cluster, Gitti et al. (2007) found that powerful outbursts are likely occurring $\sim 10\%$ of the time in most cool core clusters. NGC 193 and NGC 4261 seem to fall in to this category, with cavity powers greatly exceeding the cooling luminosity. Such systems may imply an intermittent feedback mechanism, with strong outbursts heating their surroundings enough that long periods of cooling will be required before a new fuel supply can be built up. Modeling suggests that this type of feedback can be produced by more chaotic accretion processes (e.g., Prasad et al. 2015, 2017, and references therein).

It is interesting to note that both our large-scale, high-power jet systems are found in groups whose X-ray characteristics present difficulties to analysis. NGC 4261 has an X-ray bright core, but its IGM has a relatively low surface brightness, its cavities extend beyond the *Chandra* ACIS-S3 field of view, and its cavity rims were only recognised in *XMM-Newton* observations (O’Sullivan et al. 2011; Croston et al. 2005). The outburst in NGC 193 has severely disturbed its inner X-ray halo, making the usual radial analysis difficult and somewhat uncertain. Neither system is included in the majority of X-ray selected samples of groups used to study group properties and AGN feedback. This raises the question of whether the biases implicit in X-ray selection (e.g., toward centrally-concentrated, relaxed cool-core systems, Eckert et al. 2011) may tend to exclude the more extreme cases of AGN feedback. NGC 4261 and NGC 193 are by no means

the most extreme radio galaxies hosted by groups and poor clusters. In the nearby universe, NGC 383 and NGC 315 host the giant radio sources 3C 31 and B2 0055+30, both of which have jets extending hundreds of kiloparsecs (see, e.g., Giacintucci et al. 2011). The impact of such sources on the cooling cycle is not well understood, but they suggest that caution should be exercised before concluding that feedback in groups and clusters is always a gentle process with only mild effects on IGM properties.

7 CONCLUSIONS

In this paper we have presented, for the first time, the GMRT radio images of the brightest group early-type galaxies from the high-richness CLoGS sub-sample at 235 and 610 MHz.

A high radio detection rate of 92% (24 of 26 BGEs) is found at either 235, 610 and 1400 MHz, with the majority of the BGEs exhibiting low radio powers between $10^{21} - 10^{23}$ W Hz⁻¹ with only three radio sources in the sample being characterized as radio loud ($P_{235 \text{ MHz}} > 10^{24}$ W Hz⁻¹ - NGC 4261, NGC 193 and NGC 5044). In agreement with previous studies (e.g., Magliocchetti & Brüggén 2007; Dunn et al. 2010) we confirm the trend suggesting that nearly all dominant galaxies in groups or clusters are hosting a central radio source.

The extended radio sources in our sample have spatial scales spanning the range $\sim 10 - 240$ kpc with a variety of morphologies extending over 3 orders of magnitude in power, from 10^{21} W Hz⁻¹ (NGC 5982), to 6×10^{24} W Hz⁻¹ (NGC 4261). The majority of our systems (14/26, $\sim 53\%$) exhibit a point-like radio morphology, while 6/26 groups ($\sim 23\%$) host currently or recently active small/large scale jets, and 4/26 groups (15%) host diffuse radio sources.

We find that the unresolved point-like radio sources are mainly AGN dominated with the stellar population most probably contributing in the radio emission between 20 – 40% in 3 systems (NGC 940, NGC 2563, NGC 5982) and most likely dominating in another one (NGC 584).

Comparing the X-ray environment in which the BGEs reside with their radio emission we find a distinction between central radio sources in X-ray bright and faint groups. All but one of the jet sources are found in X-ray bright cool-core systems, confirming that the X-ray bright groups or clusters are the preferred environment for radio jets to appear even down to the lower mass range covered by our sample. On the other hand, all galaxies that lack radio emission are found in X-ray faint systems. Low power radio point-like sources are found to be common in both environments.

We find that 19/26 galaxies are detected at both 610 and 235 MHz with 2/19 sources exhibiting steep radio spectra with $\alpha_{235}^{610} > 1$ (NGC 1587 and NGC 5044). The spectral indices of the remaining 17/19 sources cover the range $\alpha_{235}^{610} \approx 0.2 - 0.9$ with a mean of $\alpha_{235}^{610} = 0.53 \pm 0.16$. The equivalent mean value 235-1400 MHz spectral index for the 18/26 BGEs that exhibit emission at both frequencies, is measured to be $\alpha_{235}^{1400} = 0.60 \pm 0.16$. In X-ray bright groups, the radio sources are found to have steeper spectral indices than the mean α_{235}^{1400} .

The mean spiral fraction (F_{sp}) per radio morphology shows that radio point-like emission appears preferably in group systems where the majority of galaxies is spirals with this mild trend being stronger towards lower X-ray luminosity systems.

Considering the origin of the radio emission in our diffuse sources, their range of spectral indices, morphologies and scales means that no single mechanism seems able to explain all the

sources. We rule out star formation as the dominant factor, but it could, along with disrupted jets, aged and distorted radio lobes from past outbursts, and material shocked or compressed by galaxy interactions, potentially make a contribution.

Considering the energetics of the radio jet sources, we find mechanical power values (P_{cav}) typical for galaxy groups, in the range $\sim 10^{41} - 10^{43}$ with our systems being in good agreement with other group-central sources (e.g., Birzan et al. 2008; O’Sullivan et al. 2011).

Lastly, we find that small scale jet systems are able to balance cooling in the central region of the group provided that the AGN continuously injects energy, in agreement with Panagoulia et al. (2014), whereas the mechanical power output of the two large scale systems in our sample (NGC 193 and NGC 4261) appears to exceed the cooling X-ray luminosity of their environment by a factor of ~ 100 . This suggests that while in some groups thermal regulation can be achieved by a relatively gentle, ‘bubbling’, feedback mode, considerably more violent AGN outbursts can also take place, which may effectively shut down the central engine for long periods.

8 ACKNOWLEDGMENTS

The GMRT staff are gratefully acknowledged for their assistance during data acquisition for this project. GMRT is run by the National Centre for Radio Astrophysics of the Tata Institute of Fundamental Research. E. O’Sullivan acknowledges support for this work from the National Aeronautics and Space Administration through Chandra Awards GO6-17121X and GO6-17122X, issued by the Chandra X-ray Observatory Center, which is operated by the Smithsonian Astrophysical Observatory for and on behalf of NASA under contract NAS8-03060, and through the Astrophysical Data Analysis programme, award NNX13AE71G. S. Giacintucci acknowledges support for basic research in radio astronomy at the Naval Research Laboratory by 6.1 Base funding. M. Gitti acknowledges partial support from PRIN-INAF 2014. A. Babul acknowledges support by NSERC (Canada) through the discovery grant program. Some of this research was supported by the EU/FP7 Marie Curie award of the IRSES grant CAFE-GROUPS (247653). We acknowledge the usage of the HyperLeda database (<http://leda.univ-lyon1.fr>). This research has made use of the NASA/IPAC Extragalactic Database (NED) which is operated by the Jet Propulsion Laboratory, California Institute of Technology, under contract with the National Aeronautics and Space Administration.

REFERENCES

- Allen S. W., Dunn R. J. H., Fabian A. C., Taylor G. B. and Reynolds C. S., 2006, MNRAS, 372, 21
- Andreon S. and Moretti A., 2011, A&A, 536, 37
- Baldi R. D. and Capetti A., 2009, A&A, 508, 603
- Balogh M. L., Mazzotta P., Bower R. G., Eke V., Bourdin H., Lu T. and Theuns T., 2011, MNRAS, 412, 947
- Bardelli S., Schinnerer E., Smolčić V., Zamorani G., Zucca E., Mignoli M., Halliday C., 2010, A&A, 511A, 1
- Becker R. H., White R. L. and Helfand D. J., 1995, ApJ, 450, 559
- Beers T. C., Flynn K. and Gebhardt K., 1990, AJ, 100, 32
- Bekki K., Shioya Y. and Tanaka I., 1999, ApJ, 520, 99

- Berlind A. A., Frieman J., Weinberg D. H., Blanton M. R., Warren M. S., Abazajian K. et al., 2006, *ApJS*, 167, 1
- Best P. N., Kauffmann G., Heckman T. M., Brinchmann J., Charlot S., Ivezić Ž and White S. D. M., 2005, *MNRAS*, 362, 25
- Bharadwaj V., Reiprich T. H., Schellenberger G., Eckmiller H. J., Mittal R. and Israel H., 2014, *A&A*, 572, 46
- Birkinshaw M., Davies R. L., 1985, *ApJ*, 291, 32
- Birzan L., Rafferty D. A., McNamara B. R., Wise M. W. and Nulsen P. E. J., 2004, *ApJ*, 607, 800
- Birzan L., McNamara B. R., Nulsen P. E. J., Carilli C. L. and Wise M. W., 2008, *ApJ*, 686, 859
- Birzan L., Rafferty D. A., Nulsen P. E. J., McNamara B. R., Röttgering H. J. A., Wise M. W. and Mittal R., 2012, *MNRAS*, 427, 3468
- Bitsakis T., Charmandaris V., Le Floc’h E., Díaz-Santos T., Slater S. K., Xilouris E. and Haynes M. P., 2010, *A&A*, 571, 75
- Bitsakis T., Charmandaris V., Appleton P. N., Díaz-Santos T., Le Floc’h E., da Cunha E., Alatalo K. and Cluver M., 2014, *A&A*, 565, 25
- Borne K. D. and Hoessel J. G., 1988, *ApJ*, 330, 51
- Bogdán Á., van Weeren R. J., Kraft R. P., Forman W. R., Randall S., Giacintucci S., 2014, *ApJ*, 782, 19
- Böhringer H., Voges W., Huchra J. P., McLean B., Giacconi R., Rosati P., Burg R., Mader J., Schuecker P. et al., 2000, *ApJS*, 129, 435
- Böhringer H., Schuecker P., Guzzo L., Collins C. A., Voges W., Cruddace R. G., Ortiz-Gil A., Chincarini G., et al., 2004, *A&A*, 425, 367
- Bornancini C. G., O’Mill A. L., Gurovich S. and Lambas D. G., 2010, *MNRAS*, 406, 197
- Brienza M., Morganti R., Shulevski, Godfrey L. and Vilchez N., 2016, *AN*, 337, 31
- Brown M. J. I., Jannuzi B. T., Floyd D. J. E. and Mould J. R., 2011, *ApJ*, 731, 41
- Brunetti G. and Jones T. W., 2014, *IJMPD*, 2330007, arXiv:1401.7519
- Capak P., Aussel H., Ajiki M., McCracken H. J., Mobasher B., Scoville N. and Shopbell P., 2007, *ApJS*, 172, 99
- Carignan C., Cote S., Freeman K. C. and Quinn P. J., 1997, *AJ*, 113, 1585
- Cavagnolo K. W., McNamara B. R., Nulsen P. E. J., Carilli C. L., Jones C. and Birzan L., 2010, *ApJ*, 720, 1066
- Chandra P., Ray A. and Bhatnagar S., 2004, *ApJ*, 612, 974
- Combes, F., 2015, *IInst*, 10, C09001
- Condon J. J., 1992, *ARA&A*, 30, 575
- Condon J. J., Cotton W. D., Greisen E. W., Yin Q. F., Perley R. A., Taylor G. B. and Broderick J. J., 1998, *AJ*, 115, 1693
- Condon J. J. and Cotton W. D., 2002, *AJ*, 124, 675
- Cotton W. D., Wittels J. J., Shapiro I. I., Marcaide J., Owen F. N., Spangler S. R., 1980, *ApJ*, 238, 123
- Croston, J. H., Hardcastle, M. J. and Birkinshaw, M., 2005, *MNRAS*, 357, 279
- David L. P., O’Sullivan E., Jones C., Forman W., Nulsen P., Vrtilek J., O’Sullivan E., Giacintucci S. and Raychaudhury S., 2009, *ApJ*, 705, 624
- David L. P., O’Sullivan E., Jones C., Giacintucci S., Vrtilek J., Raychaudhury S., Nulsen P. E. J. Forman W., Sun M. and Donahue M., 2011, *ApJ*, 728, 162
- David L. P., Lim J., Forman W., Vrtilek J., Combes F., Salome P., Edge A., Hamer S., Jones C., Sun M., O’Sullivan E., et al., 2014, *ApJ*, 792, 14
- David, L. P., Vrtilek, J., O’Sullivan, E., Jones, C., Forman, W. and Sun, M., 2017, *ApJ*, 842, 84
- de Vaucouleurs G., de Vaucouleurs A., Corwin Jr. H. G., Buta R. J., Paturel G. and Fouqué P., 1991, *rc3*, book, D
- de Zotti G., Massardi M., Negrello M., Wall J., 2010, *A&ARv*, 18, 1
- Del Burgo C., Carter D., Sikkema G., 2008, *A&A*, 477, 105
- Dong R., Rasmussen J. and Mulchaey J. S., 2010, *ApJ*, 712, 883
- Doria A., Gitti M., Ettori S., Brighenti F., Nulsen P. E. J. and McNamara B. R., 2012, *ApJ*, 753, 47
- Dressler A. and Condon, J. J., 1978, *ApJS*, 36, 53
- Dunn R. J. H. and Fabian A. C., 2006, *MNRAS*, 373, 959
- Dunn R. J. H., Allen S. W., Taylor G. B., Shurkin K. F., Gentile G., Fabian A. C. and Reynolds C. S., 2010, *MNRAS*, 404, 180
- Durand N., Bottinelli L., Gouguenheim L., Paturel G., Garnier R., Marthinet M. C., Petit C., 1994, *ASPC*, 67, 281
- Ebeling H., Edge A. C., Allen S. W., Crawford C. S., Fabian A. C. and Huchra J. P., 2000, *MNRAS*, 318, 333
- Eckert D., Molendi S. and Paltani S., 2011, *A&A*, 526, 79
- Eckmiller H. J., Hudson D. S., & Reiprich T. H., 2011, *A&A*, 535, 105
- Edge A. C., Stewart G. C., Fabian A. C. and Arnaud K. A., 1990, *MNRAS*, 245, 559
- Eke V. R., Baugh C. M., Cole S., Frenk C. S., Norberg P., Peacock J. A., Baldry I. K., Bland-Hawthorn J., Bridges T., Cannon R., Colless M., Collins C., Couch W., Dalton G., de Propris R., Driver S. P., Efstathiou G. et al., 2004, *MNRAS*, 348, 866
- Eke V. R., Baugh C. M., Cole S., Frenk C. S., King H. M. and Peacock J. A., 2005, *MNRAS*, 362, 1233
- Eskridge P. B. and Pogge R. W., 1991, *AJ*, 101, 2056
- Fabian A. C., Sanders J. S., Taylor G. B., Allen S. W., Crawford C. S., Johnstone R. M., Iwasawa K., 2006, *MNRAS*, 366, 417
- Fabian A. C., 2012, *ARA&A*, 50, 455
- Fanaroff B. L., Riley J. M., 1974, *MNRAS*, 167, 31P
- Fanti C., Fanti R., Dallacasa D., Schilizzi R. T., Spencer R. E. and Stanghellini C., 1995, *A&A*, 302, 317
- Feretti L. and Giovannini G., 2008, *LNP*, 740, 143
- Feretti L., Giovannini G., Govoni F. and Murgia M., 2012, *A&ARv*, 20, 54
- Ferrari C., Govoni F., Schindler S., Bykov A. M., Rephaeli Y., 2008, *SSRv*, 134, 93
- Filho M. E., Barthel P. D. and Ho L. C., 2002, *ApJ*, 142, 223
- Forbes D. A., Ponman T., Pearce F., Osmond J., Kilborn V., Brough S., Raychaudhury S., Mundell C., Miles T. and Kern K., 2006, *PASA*, 23, 38
- Fukugita M., Hogan C. J. and Peebles P. J. E., 1998, *ApJ*, 503, 518
- Garcia A. M., 1993, *A&AS*, 100, 47
- Garn T., Green D. A., Riley J. M. and Alexander P., 2009, *MNRAR*, 397, 1101
- Gaspari M., Brighenti F., D’Ercole A., Melioli C., 2011, *MNRAS*, 415, 1549
- Gastaldello F., Di Gesu L., Ghizzardi S., Giacintucci S., Girardi M., Roediger E., 2013, *ApJ*, 770, 56
- Geller M. J. and Huchra J. P., 1983, *ApJS*, 52, 61
- Giacintucci S., Venturi T., Murgia M., Dallacasa D., Athreya R., Bardelli S., Mazzotta P. and Saikia D. J., 2007, *A&A*, 476, 99
- Giacintucci S., O’Sullivan E., Vrtilek J., David L. P., Raychaudhury S., Venturi T., Athreya R. M., Clarke T. E., Murgia M., Mazzotta P., Gitti M., Ponman T. et al., 2011, *ApJ*, 732, 95
- Giacintucci S., Markevitch M., Cassano R., Venturi T., Clarke T. E. and Brunetti G., 2017, *ApJ*, 841, 71
- Giodini S., Pierini D., Finoguenov A., Pratt G. W., Boehringer H.,

- Leauthaud A., Guzzo L., Aussel H., Bolzonella M., Capak P., Elvis M., Hasinger G. et al., 2009, *ApJ*, 703, 982
- Giroletti M., Giovannini G. and Taylor G. B., 2005, *AAP*, 441, 89
- Gitti M., McNamara B. R., Nulsen P. E. J. and Wise M. W., 2007, *ApJ*, 660, 1118
- Gitti M., Brighenti F. and McNamara B. R., 2012, *AdAst*, 2012, 6
- Gitti M., Tozzi P. Brunetti G., Cassano R., Dallacasa D., Edge A., Etori S., Feretti L. et al., 2015, *AASKA14, confE*, 76
- González-Martín O., Masegosa J., Márquez I., Guainazzi M. and Jiménez-Bailón E., 2009, *AAP*, 506, 1107
- Goto T. et al., 2003, *PASJ*, 55, 757
- Govoni F., Enßlin T.A., Feretti L. and Giovannini G. 2001, *A&A*, 369, 441
- Guo F. and Oh S. P., 2009, *MNRAS*, 400, 1992
- Haines C. P., Finoguenov A., Smith G. P., Babul A., Egami E., Mazzotta P., Okabe N., Pereira M. J., 2017, *arXiv*, 1709.04945
- Hashimoto Y. and Oemler Jr. A., 2000, *ApJ*, 530, 652
- Millennium Star Atlas Vol II Chart 655, Sky Atlas 2000 Chart 7, Uranometria 2000 Vol I Chart 107, Herald-Bobroff AstroAtlas B-05 C-21
- Hickson P., 1982, *ApJ*, 255, 382
- Hickson P., Mendes de Oliveira, C., Huchra, J. P. and Palumbo, G. G., 1992, *ApJ*, 399, 353
- Hickson P., 1997, *ARA&A*, 35, 357
- Hlavacek-Larrondo J., Fabian A. C., Edge A. C., Ebeling H., Sanders J. S., Hogan M. T. and Taylor G. B.
- Ho L. C. and Ulvestad J. S., 2001, *ApJS*, 133, 77
- Ho L. C., Filippenko A. V. and Sargent W. L. W., 1997, *ApJS*, 112, 315
- Hogan M. T., Edge A. C., Hlavacek-Larrondo J., Grainge K. J. B., Hamer S. L., Mahony E. K., Russell H. R., Fabian A. C., McNamara B. R. and Wilman R. J., 2015, *MNRAS*, 453, 1201
- Hopkins P. F., Somerville R. S., Hernquist L., Cox T. J., Robertson B., Li Y., 2006, *ApJ*, 652, 864
- Huang M.-L. and Chen L.-W., 2010, *IAUS*, 267, 110
- Jarrett T. H., Masci F., Tsai C. W., Petty S., Cluver M. E., Assef R. J., Benford D., Blain A., Bridge C., Donoso E., Eisenhardt P., Koribalski B., Lake S., Neill J. D., Seibert M., Sheth K., Stanford S., Wright E., 2013, *AJ*, 145, 6
- Jenkins C. R., 1982, *MNRAS*, 200, 705
- Kale R., Venturi T., Giacintucci S., Dallacasa D., Cassano R., Brunetti G., Macario G. and Athreya R., 2013, *A&A*, 557, 99
- Kale R., Venturi T., Cassano R., Giacintucci S., Bardelli S., Dallacasa D. and Zucca E., 2015, *A&A*, 581, 23
- Karachentsev I. D., 1972, *SoSAO*, 7, 1
- Kempner J. C., Blanton E. L., Clarke T. E., Enßlin T. A., Johnston-Hollitt M. and Rudnick L., 2004, *refg, proc*, 335K
- Knapp G. R. and Rupen M. P., 1996, *ApJ*, 460, 271
- Kokotanekov G., Wise M., Heald G. H., McKean J. P., Bîrzan L., Rafferty D. A., Godfrey L. E. H., de Vries et al., 2017, *A&A*, 605, 48
- Kolokythas K., O'Sullivan E., Giacintucci S., Raychaudhury S., Ishwara-Chandra C.H., Worrall D. M. and Birkinshaw M., 2015, *MNRAS*, 14, 1422
- Kuhr H., Witzel A., Pauliny-Toth I. I. K. and Nauber U., 1981, *A&AS*, 45, 367
- Laganá T. F., Zhang Y.-Y., Reiprich T. H., Schneider P., 2011, *ApJ*, 743, 13
- Ledlow M. J., Owen F. N. and Eilek J. A., 2002, *NewAR*, 46, 343
- Liang L., Durier F., Babul A., Davé R., Oppenheimer B. D., Katz N., Fardal M. and Quinn T., 2016, *MNRAS*, 456, 4266
- Lilly S. J., Le Brun V., Maier C., Mainieri V., Mignoli M., Scodeggio M., Zamorani G., Carollo M. et al., 2009, *ApJS*, 184, 218
- Lin Y.-T. and Mohr J. J., 2007, *ApJS*, 170, 71
- Lin H. W., McDonald M., Benson B. and Miller E., 2015, *ApJ*, 802, 34
- Loubser S. I., Hoekstra H., Babul A. and O'Sullivan E., 2018, *MNRAS*, tmp, 483
- Ma C.-J., McNamara B. R., Nulsen P. E. J., Schaffer R. and Vikhlinin A., 2011, *ApJ*, 740, 51
- Ma C.-J., McNamara B. R. and Nulsen P. E. J., 2013, *ApJ*, 763, 63
- Machacek M. E., Jerius D., Kraft R., Forman W. R., Jones C., Randall S., Giacintucci S. and Sun M., 2011, *ApJ*, 743, 15
- Madore B. F., Freedman W. L. and Bothun G. D., 2004, *ApJ*, 607, 810
- Magliocchetti M. and Brüggén M., 2007, *MNRAS*, 379, 260
- Mahdavi A., Trentham and Tully R. B., 2005, *AJ*, 130, 1502
- Malavasi N., Bardelli S., Ciliegi P., Ilbert O., Pozzetti L. and Zucca E., 2015, *A&A*, 576A, 101
- Mamon G. A., 2000, *BAAS, ASPC*, 197, 377
- Martin C. and GALEX Team, 2005, *IAUS*, 216, 221
- Mazzotta P. and Giacintucci S., 2008, *ApJ*, 675, 9
- McCarthy I. G., Schaye J., Ponman T. J., Bower R. G., Booth C. M., Dalla Vecchia, et al., 2010, *MNRAS*, 406, 822
- McNamara B. R., Wise M., Nulsen P. E. J., David L. P., Sarazin C. L., Bautz M., Markevitch M., Vikhlinin A. et al., 2000, *ApJ*, 534, 135
- McNamara B. R., Nulsen P. E. J., Wise M. W., Rafferty D. A., Carilli C., Sarazin C. L. and Blanton E. L., 2005, *Natur*, 433, 45
- McNamara B. R., Nulsen P. E. J., 2007, *ARA&A*, 45, 117
- Mendes de Oliveira C., 1995, *MNRAS*, 273, 139
- Merloni A., Predehl P., Becker W., Böhringer H., Boller T., Brunner H., Brusa M., Dennerl K. et al., 2012, [*arXiv*1209.3114M]
- Miles T. A., Raychaudhury S., Forbes D. A., Goudfrooij P., Ponman T. J. and Kozhurina-Platais V., 2004, *MNRAS*, 355, 785
- Mittal R., Hudson D. S., Reiprich T. H. and Clarke T., 2009, *A&A*, 501, 835
- Moss C. and Whittle M., 2000, *MNRAS*, 317, 667
- Mulchaey J. S. and Zabludoff A. I., 1998, *ApJ*, 496, 73
- Mulchaey J. S., 2000, *ARA&A*, 38, 289
- Mulchaey J. S., Davis D. S., Mushotzky R. F. and Burstein D., 2003, *ApJ*, 145, 39
- Murgia M., Fanti C., Fanti R., Gregorini L., Klein U., Mack K.-H. and Vigotti M., 1999, *A&A*, 345, 769
- Murgia M., Parma P., Mack K.-H., de Ruiter H. R., Fanti R., Govoni F., Tarchi A., Giacintucci S. and Markevitch M., 2011, *A&A*, 526A, 148
- Nulsen P. E. J., McNamara B. R., Wise M. W., David L. P., 2005, *ApJ*, 628, 629
- Nulsen, P. E. J., Jones, C., Forman, W. R., David, L. P., McNamara, B. R., Rafferty, D. A., Bîrzan, L. and Wise, M. W., 2007, in Böhringer, H., Pratt, G. W., Finoguenov, A., Schuecker, P., eds, *Heating versus Cooling in Galaxies and Clusters of Galaxies*, Springer-Verlag, Berlin, p. 210
- Nulsen P. E. J., Jones C., Forman W., Churazov E., McNamara B., David L. and Murray S., 2009, *AIPC*, 1201, 198
- Osmond J. P. F. and Ponman T. J., 2004, *MNRAS*, 350, 1511
- O'Sullivan E., Kolokythas K., Kantharia N. G., Raychaudhury S., David L. P. and Vrtilik J. M., 2018, *MNRAS*, 473, 5248
- O'Sullivan E., Ponman T. J., Kolokythas K., Raychaudhury S., Babul A., Vrtilik J. M., David L. P., Giacintucci S., Gitti M. and Haines C. P., 2017, *MNRAS*, 472, 1482
- O'Sullivan E., Combes F., Hamer S., Salomé P., Babul A. and

- Raychaudhury S., 2015, *A&A*, 573A, 111
- O’Sullivan E., Kolokythas K., Raychaudhury S., Vrtilek J. M., Kantharia N., 2014, arXiv1402, 46760
- O’Sullivan E., David L. P. and Vrtilek J. M., 2014, *MNRAS*, 437, 730
- O’Sullivan E., Giacintucci S., David L. P., Vrtilek J. M. and Raychaudhury S., 2011, *MNRAS*, 411, 1833
- O’Sullivan E., Worrall D. M., Birkinshaw M., Trinchieri G., Wolter A., Zezas A., Giacintucci S., 2011, *MNRAS*, 416, 2916
- O’Sullivan E., Giacintucci S., Vrtilek J. M., Raychaudhury S. and David L. P., 2009, *ApJ*, 701, 1560
- Panagoulia, E. K., Fabian, A. C., Sanders, J. S. and Hlavacek-Larrondo, J., 2014, *MNRAS*, 444, 1236
- Patrel G., Petit C., Prugniel P., Theureau G., Rousseau J., Brouty M., Dubois P. and Cambrésy L., 2003, *A&A*, 412, 45
- Pearson R. J., Ponman T. J., Norberg P., Robotham A. S. G. and Farr W. M., 2015, *MNRAS*, 449, 3082
- Peres C. B., Fabian A. C., Edge A. C., Allen S. W., Johnstone R. M., White D. A., 1998, *MNRAS*, 298, 416
- Pildis R. A., Bregman J. N. and Evrard A. E., 1995, *ApJ*, 443, 514
- Pillepich A., Porciani C. and Reiprich T. H., 2012, *MNRAS*, 422, 44
- Piner B. G., Jones D. L., Wehrle A. E., 2001, *AJ*, 122, 2954
- Ponman T. J., Bourner P. D. J., Ebeling H. and Böhringer H., 1996, *MNRAS*, 283, 690
- Prasad D., Sharma P. and Babul A., 2015, *ApJ*, 811, 108
- Prasad D., Sharma P. and Babul A., 2017, *MNRAS*, 471, 1531
- Rafferty D. A., McNamara B. R., Nulsen P. E. J. and Wise M. W., 2006, *ApJ*, 652, 216
- Rafferty D. A., Birzan L., Nulsen P. E. J., McNamara B. R., Brandt W. N., Wise M. W., Röttgering H. J. A., 2013, *MNRAS*, 428, 58
- Randall S. W., Jones C., Kraft R., Forman W. R. and O’Sullivan E., 2009, *ApJ*, 696, 1431
- Randall S. W., Forman W. R., Giacintucci S., Nulsen P. E. J., Sun M., Jones C., Churazov E., et al., 2011, *ApJ*, 726, 86
- Rasmussen J., Ponman T. J., Mulchaey J. S., Miles T. A. and Raychaudhury S., 2006, *MNRAS*, 373, 653
- Rasmussen J., Bai X.-N., Mulchaey J. S., van Gorkom J. H., Jeltema T. E., Zabludoff A. I., Wilcots E., Martini P., Lee D., Roberts T. P., 2012, *ApJ*, 747, 31
- Reiprich T. H. and Böhringer H., 2002, *ApJ*, 567, 716
- Rest A., van den Bosch F. C., Jaffe W., Tran H., Tsvetanov Z., Ford H. C., Davies J., Schafer J., 2001, *AJ*, 121, 2431
- Salim S., Rich R. M., Charlot S., Brinchmann J., Johnson B. D., Schiminovich D., Seibert M., Mallery R. et al., *ApJS*, 173, 267
- Salvato M., Hasinger G., Ilbert O., Zamorani G., Brusa M., Scoville N. Z., Rau A., Capak P., 2009, *ApJ*, 690, 1250
- Sanderson A. J. R., Ponman T. J. and O’Sullivan E., 2006, *MNRAS*, 372, 1496
- Sanghera H. S., Saikia D. J., Luedke E., Spencer R. E., Foulsham P. A., Akujor C. E. and Tzioumis A. K., 1995, *AAP*, 295, 629
- Schweizer F. and Seitzer P., 1992, *AJ*, 104, 1039
- Shabala S. S., Ash S., Alexander P. and Riley J. M., 2008, *MNRAS*, 388, 625
- Shen Y., Mulchaey J. S., Raychaudhury S., Rasmussen J. and Ponman T. J., 2007, *ApJ*, 645, 115
- Shulevski A., Morganti R., Oosterloo T. and Struve C., 2012, *AAP*, 545, 91
- Stott J. P., Collins C. A., Sahlén M., Hilton M., Lloyd-Davies E., Capozzi D. et al., 2010, *ApJ*, 718, 23
- Sun M., 2009, *AIPC*, 1201, 210
- Sun M., 2012, *NJPh*, 14d5004S
- Taylor J. E. and Babul A., 2005, *MNRAS*, 364, 515
- Toomre A. and Toomre J., 1972, *BAAS*, 4, 214
- Trager S. C., Faber S. M., Worthey G. and González J. J., 2000, *AJ*, 119, 1645
- Trinchieri G., Fabbiano G. and Kim D.-W., 1997, *A&A*, 318, 361
- Trinchieri G. and Goudfrooij P., 2002, *A&A*, 386, 472
- Tully R. B., 1987, *ApJ*, 321, 280
- Tully R. B. and Trentham N., 2008, *AJ*, 135, 1488
- Vajgel B., Jones C., Lopes P. A. A., Forman W. R., Murray S. S., Goulding A., Andrade-Santos F., 2014, *ApJ*, 794, 88
- van den Bosch F. C., Jiang F., Hearin A., Campbell D., Watson D. and Padmanabhan N., 2014, *MNRAS*, 445, 1713
- van Driel W. and van Woerden H., 1991, *AAP*, 243, 71
- Venturi T., Giacintucci S., Brunetti G., Cassano R., Bardelli S., Dallacasa D. and Setti G., 2007, *A&A*, 463, 937
- Venturi T., Giacintucci S., Dallacasa D., Cassano R., Brunetti G., Bardelli S. and Setti G., 2008, *A&A*, 484, 327
- Vollmer B., Cayatte V., Balkowski C. and Duschl W. J., 2001, *ApJ*, 561, 708
- von der Linden A., Best P. N., Kauffmann G. and White S. D. M., 2007, *MNRAS*, 379, 867
- Weilbacher P. M., Duc P.-A., Fritze v. Alvensleben U., Martin P., Fricke K. J., 2000, *AAP*, 358, 819
- Wise M. W., McNamara B. R. and Murray S. S., 2004, *ApJ*, 601, 184
- Worrall D. M., Birkinshaw M., O’ Sullivan E., Zezas A., Wolter A., Trinchieri G., Fabbiano G., 2010, *MNRAS*, 408, 701
- Yang X., Mo H. J., van den Bosch F. C., Jing Y. P., Weinmann S. M., Meneghetti M., 2006, *MNRAS*, 373, 1159
- Yuan Z. S., Han J. L. and Wen Z. L., 2016, *MNRAS*, 460, 3669
- Zeilinger W. W., Pizzella A., Amico P., Bertin G., Bertola F., Buson L. M. et al., 1996, *A&AS*, 120, 257
- Zeilinger W. W., Galletta G. and Madsen C., 1990, *MNRAS*, 246, 324
- Zhao Y.-H., Gu Q.-S., Peng Z.-X., Shi L., Luo X.-L., Peng Q.-H., 2006, *ChJAA*, 6, 15

APPENDIX A: GMRT RADIO CONTINUUM IMAGES

In this appendix we provide *Chandra* or *XMM* X-ray and Digitized Sky Survey optical images of our BGEs, with 610 (cyan) and 235 MHz (green) contours overlaid, as well as notes on relevant features of each galaxy and radio source. In all figures, the panels on the left represent the X-ray images overlaid by the 235 MHz contours, and the panels on the right, the optical images overlaid by the 610 MHz contours.

A1 NGC 410

NGC 410 is the BGE of the X-ray luminous LGG 18 group. A central point source was detected at 1.4 GHz (in the NVSS catalog Condon et al. 1998) and at 8.4 GHz (Filho et al. 2002), with flux densities of 6.3 mJy and 1.7 mJy respectively. Figure A1 shows the point-like radio source detected in both GMRT frequencies, located coincident with the optical centroid, with some hint of a small extension to the northeast in the 610 MHz emission.

González-Martín et al. (2009) class the galaxy nucleus as a low-ionization emission region (LINER), but argue that it is not an AGN based on a combination of X-ray, UV, H α and radio data.

A2 NGC 584

NGC 584 is the dominant member of a small group of galaxies, LGG 27, and is thought to have recently undergone a merger (Trager et al. 2000), with evidence of ongoing star formation Schweizer et al. (2000). Madore et al. (2004) argue that NGC 584 does not lie at the gravitational centre of its group.

Although identified with a low-power source in NVSS, NGC 584 is undetected in our GMRT observations. Two nearby bright background sources (~ 5 and ~ 7 Jy at 235 MHz) produce an enhanced noise level in the central part of our images, leading us to set the detection limit at 5σ . The radio contours overlapping the optical body of the galaxy in figure A2 appear to be noise rather than detected sources. Our X-ray observations detected no hot gas associated with the group or galaxy.

A3 NGC 677

NGC 677 is located at the centre of the X-ray luminous group LGG 31. The galaxy has a LINER nucleus (Zhao et al. 2006) and was detected in the NVSS and both our GMRT observations. We observe a central point source surrounded by irregular diffuse emission extending ~ 30 kpc at 610 MHz. The morphologies at 235 and 610 MHz are inconsistent, with the 235 MHz emission presenting an asymmetric bipolar morphology overlapping the more rounded 610 MHz emission. These morphological differences may arise from differences in relative sensitivity to low surface-brightness emission at the two frequencies particularly if spectral index varies across the source (i.e., if the regions detected at 235 MHz represent only the most luminous, steepest spectrum regions of the more extended source seen at 610 MHz).

A4 NGC 777

NGC 777, BGE of the LGG 42 group, is classed by Ho et al. (1997) as a slow-rotating Seyfert 2 galaxy, having a population of very old stars (Jarrett et al. 2013). Earlier observations by Ho & Ulvestad (2001) reveal a marginally resolved radio source in the core, slightly extended to hint at jets. NGC 777 is at the centre of a

group-scale X-ray halo and is detected at both GMRT frequencies, presenting an asymmetric structure of ~ 6 kpc only at 235 MHz, south-west from the centre.

We examined the elongated feature at 235 MHz (see A4), making images with natural weighting (equal weight to all samples, good for tracing extended emission; *robust* parameter 5 in AIPS) and creating lower resolution images ($19.86'' \times 13.94''$, rms ~ 0.8 mJy). This revealed that the elongated feature is related to artifacts extending from northwest to southeast surrounding the central radio source, owing to systematic noise that leads to poor calibration with the data we have in hand. The upper limit of the spectral index in this area (using a 3σ significance at 610 MHz) is $\gtrsim 2.5$ which is very steep and argues against a jet emission for NGC 777.

A5 NGC 940

Previous single dish 2.38 GHz observations of NGC 940 found only a tentative detection with flux density of 5 ± 4 mJy (Dressler & Condon 1978). We detect the galaxy at both GMRT frequencies, finding a point-like radio source with an inverted spectral index α_{235}^{610} of ~ -0.3 . No hot gas halo is detected in the X-rays, and the galaxy is found to be point source dominated. The inverted spectral index could be attributed to absorption of the lower frequency emission, along with contribution from SF.

A6 NGC 924

NGC 924 is the BGE of the X-ray faint group LGG 61 and was previously undetected in the radio regime. We detect a weak radio point source associated with NGC 924 only at 610 MHz, with an upper limit of 1.5 mJy at 5σ level of significance for 235 MHz (Table 2).

A7 NGC 978

NGC 978 is the BGE of the X-ray faint LGG 66 group. It forms a galaxy pair with MCG+05-07-017 but shows no signs of interaction or distortion in optical imaging (Karachentsev 1972). The galaxy has no previous radio detection but we detect a weak radio point source at 610 MHz that coincides with the optical centre of the galaxy, with a flux density of just 1.3 mJy, one of the weakest in our sample.

A8 NGC 1060

NGC 1060 is the BGE in LGG 72 group, a strongly interacting, possibly merging X-ray bright system. Our 610 MHz image reveals a small scale jet (see figure A8) coincident with the optical centre of the galaxy. At 235 MHz this structure is unresolved. The source presents a moderately steep spectral index of ~ 0.9 . The system in X-rays presents a long arc-like path connecting NGC 1060 and NGC 1066, suggestive of a group-group merger (see O'Sullivan et al. 2017), raising the possibility that tidal interactions may have triggered the nuclear activity in NGC 1060.

A9 NGC 1167

NGC 1167 is the BGE of the X-ray faint LGG 80 group, and hosts the radio source B2 0258+35. Previous radio observations

have revealed this to be a complex, multi-scale source, with multiple sets of radio lobes. The nuclear source is classed as a young, compact steep spectrum (CSS) source (Sanghera et al. 1995), with VLA 8 and 22 GHz imaging showing a parsec-scale core with small plume-like lobes and no evidence of hotspots (Giroletti et al. 2005). VLBI 1.6 GHz observations show that the faint compact core (7.6 mJy), is surrounded by a bright diffuse region coincident with the peak of the VLA images. The diffuse component has a spectral index of $\alpha_{0.08}^{22} \sim 1.0 - 1.5$, while the core is flatter (~ 0.6 , Giroletti et al. 2005). However, these small-scale structures are dwarfed by the 240 kpc double-lobed structure detected at 1.4 GHz using the Westerbork Synthesis Radio Telescope (WSRT), which clearly indicates a much more powerful period of activity in the recent past (Shulevski et al. 2012).

Our GMRT observations detect the central source at both frequencies, with extensions to both east and west at 235 MHz (see Figure A9), potentially representing jets associated with the large-scale remnant lobes, or some intermediate period of activity. We find a total spectral index of $\alpha_{235}^{610} = 0.59$, and a value for the core similar to the one from Giroletti et al. (2005) ($\alpha_{235}^{610} = 0.55$).

A10 NGC 1453

NGC 1453 is a LINER galaxy (Zeilinger et al. 1996), located in the centre of the X-ray luminous LGG 103 group. Previous observations at 1.4 GHz detected a point-like radio source of 28 mJy (Table 2). Our images at 610 MHz and 235 MHz (see figure A10) show a compact radio point-like source at both GMRT frequencies that coincides with the central region of the optical galaxy. The spectral index of $\alpha_{235}^{610} \sim 0.2$ indicates that the radio emission possibly originates from a young AGN.

A11 NGC 2563

NGC 2563 is the BGE of the X-ray bright LGG 158 group. We detect a weak point-like radio source at 610 MHz, coincident with the centre of the optical component, but the galaxy is undetected at 235 MHz. Previous VLA observations from Brown et al. (2011) found a very weak point source at 1.4 GHz.

A12 NGC 3078

NGC 3078, in the X-ray faint LGG 185, hosts a nuclear dust disk (Rest et al. 2001) and a previously detected, relatively strong radio AGN (310 mJy source at 1.4 GHz). Figure A12 shows the source at both GMRT frequencies. It presents a symmetric diffuse structure along an east-west axis, with no clear indication of jets and separated lobes from the central component. The eastern structure appears somewhat broader than the west and overall the source is less extended at 610 MHz than at 235 MHz. The radio source presents a spectral index of $\alpha_{235}^{610} \sim 0.5$.

A13 NGC 4008

NGC 4008 is the HI-rich (Eskridge et al. 1991) BGE of the X-ray faint LGG 262 group. NVSS observations detect a weak point radio source, and our GMRT images in Figure A13 show a slightly elongated point-like radio source at both frequencies.

A14 NGC 4169

NGC 4169 is the BGE in the X-ray faint group HCG 61 (LGG 276). Previous observations from NVSS detect a very weak radio point source of ~ 1 mJy. We detect a radio point source coincident with the center of NGC 4169 with a flux density of 3 mJy at 610 MHz, but no detection is seen at 235 MHz. The upper limit for the 235 MHz detection is placed at ≤ 6 mJy, at 5σ level of significance. We note here that the repetitive patterns in the radio source of NGC 4175, are most probably due to residual amplitude and/or phase calibration errors. However the angular separation of NGC 4169 is far enough for these errors to affect the measured flux density of our source at 610 MHz.

A15 ESO 507-25

ESO 507-25 is the BGE of the X-ray faint LGG 310 group. A weak (24 mJy) nuclear source was detected at 1.4 GHz (Brown et al. 2011), and a weak broad CO emission line (Knapp et al. 1996) provides evidence of cold gas in the galaxy. At 610 MHz we observe a central point source surrounded by an asymmetric diffuse component with separated clumps of emission north and south of the central region of the galaxy. At 235 MHz no diffuse component is detected but only a compact central point source, with a hint of extension to the north-east. The source exhibits a very flat spectral index ($\alpha_{235}^{610} = 0.18$).

A16 NGC 5084

NGC 5084 is the BGE in the X-ray faint LGG 345 group, and probably recently underwent a merger with a gas-rich dwarf companion (Zeilinger et al. 1990), as shown by distorted inner isophotes (Carignan et al. 1997) and a high HI mass ($M_{(HI)}/L_{(B)} \sim 0.35$; vanDriel et al. 1991). The galaxy hosts a nuclear radio point source in the NVSS, with a flux density of 46.6 mJy.

At both GMRT frequencies, we detect a radio point source that coincides with the central region of the galaxy, presenting some hints of extension in the east–west direction. However, noise features owing to imperfect calibration are responsible for the detached clumps of emission east and west of the core in Figure A16, and we therefore consider only the central point-like structure as reliable. A flux density of 36.2 mJy at 610 MHz and 53.9 mJy at 235 MHz give a relatively flat spectral index of $\alpha \sim 0.4$ for this source at this frequency range.

A17 NGC 5153

NGC 5153 is the BGE in the X-ray faint LGG 351 group and is interacting with the spiral galaxy NGC 5152 (Weilbacher et al. 2000). There is no previous radio measurement for this system and no emission is also detected by our GMRT observations.

A18 NGC 5353

NGC 5353 is an edge-on S0 galaxy laying in the dynamical centre of the X-ray bright LGG 363 group (HCG 68, Hickson 1982) being part of the group’s dominant pair suspected to be in the process of merging (Tully et al. 2008). Point radio sources with flux densities of 41 mJy in NGC 5353 and of 8.4 mJy in NGC 5354 are reported in the NVSS. Our GMRT observations detect compact point radio sources in both galaxies. The presence of a strong background source nearby produces high noise levels at 610 MHz,

adding false structures symmetrically distributed in the east–west direction around NGC 5353. We therefore start the 610 MHz contours shown in Figure A18 at the 4σ level of significance.

A19 NGC 5846

NGC 5846 is the BGE in the X-ray luminous massive LGG 393 group of galaxies (see Mahdavi et al. 2005). Using the GMRT at 610 MHz, Giacintucci et al. (2011) detected a nuclear source with small scale jets of size of ~ 12 kpc. In our 235 MHz observations we detect a compact point radio source that coincides with the central region of the optical galaxy, with hints of extension on an east–west axis, but the resolution is not sufficient to trace the jets seen at 610 MHz. X-ray observations reveal a number of structures in the group core, including cavities (e.g., Allen et al. 2006; Dong et al. 2010) and evidence of sloshing (Machacek et al. 2011).

A20 NGC 5982

LGG 402 is a relatively poor X-ray luminous group dominated by the elliptical NGC 5982 (possibly post-merger; Del Burgo, Carter, & Sikkema 2008) and the two large spiral galaxies that lie close by (the ‘Draco Trio’). GMRT 610 and 235 MHz observations (Figure A20) detect a weak, point-like radio source at the center of the NGC 5982. Previous 1.4 GHz observations found only hints of this central source (Brown et al. 2011).

A21 NGC 6658

NGC 6658 is an edge-on S0 type BGE in the X-ray faint LGG 421 poor group of galaxies. The galaxy was not previously detected in the radio band and our GMRT observations find no radio detection at either frequency (fig. A21). The flux density upper limit set for this galaxy at 5σ level of significance is 0.3 mJy at 610 MHz and 3 mJy at 235 MHz. Figure A21 shows only a point source detected in the spiral companion NGC 6660.

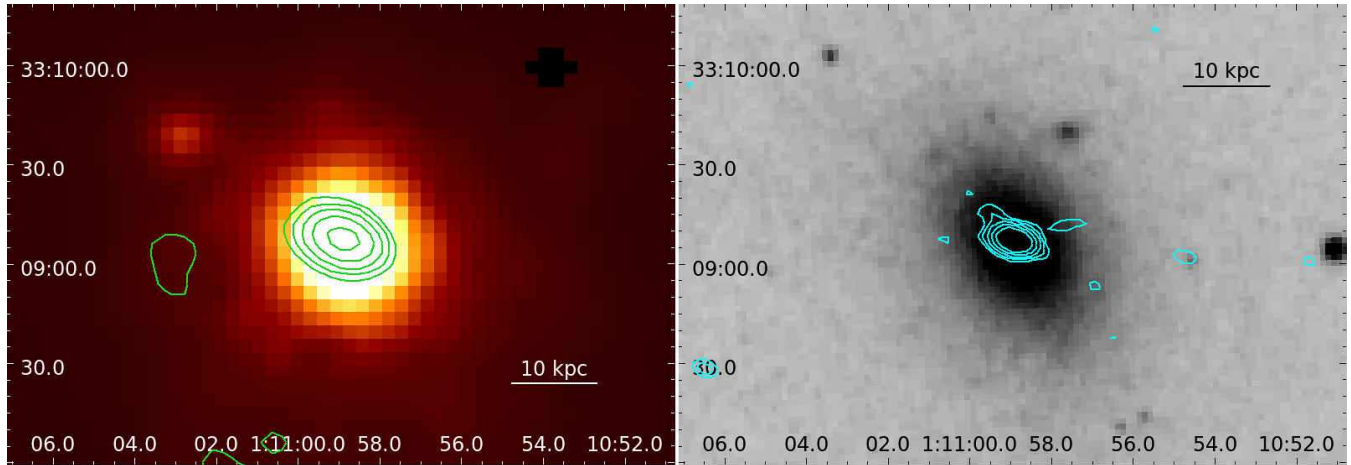


Figure A1. LGG 18 / NGC 410. *Left:* GMRT 235 MHz contours in green ($1\sigma = 0.4 \text{ mJy beam}^{-1}$), overlaid on the adaptively smoothed 0.3–2.0 keV *XMM-Newton* image. *Right:* GMRT 610 MHz contours in cyan ($1\sigma = 50 \mu\text{Jy beam}^{-1}$), overlaid on the *Digitized Sky Survey (DSS)* optical image. In both panels the radio contours are spaced by a factor of two, starting from 3σ . For this source the scale is $0.373 \text{ kpc arcsec}^{-1}$.

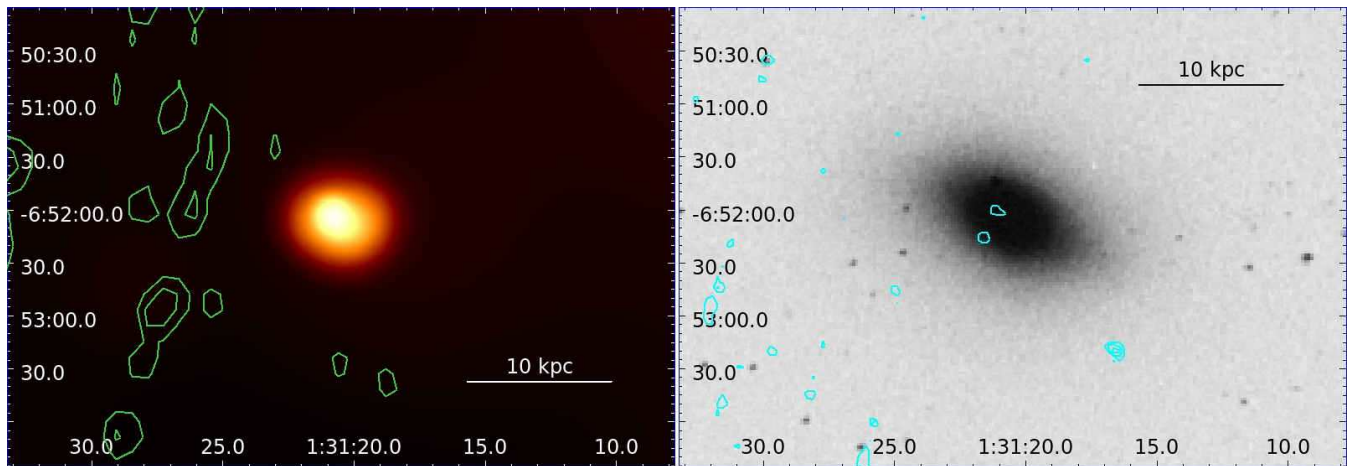


Figure A2. LGG 27 / NGC 584. *Left:* GMRT 235 MHz contours in green ($1\sigma = 1.2 \text{ mJy beam}^{-1}$), overlaid on the adaptively smoothed 0.3–2.0 keV *Chandra* image. *Right:* GMRT 610 MHz contours in cyan ($1\sigma = 200 \mu\text{Jy beam}^{-1}$), overlaid on the *DSS* optical image. In both panels the radio contours are spaced by a factor of two, starting from 3σ . For this source the scale is $0.121 \text{ kpc arcsec}^{-1}$.

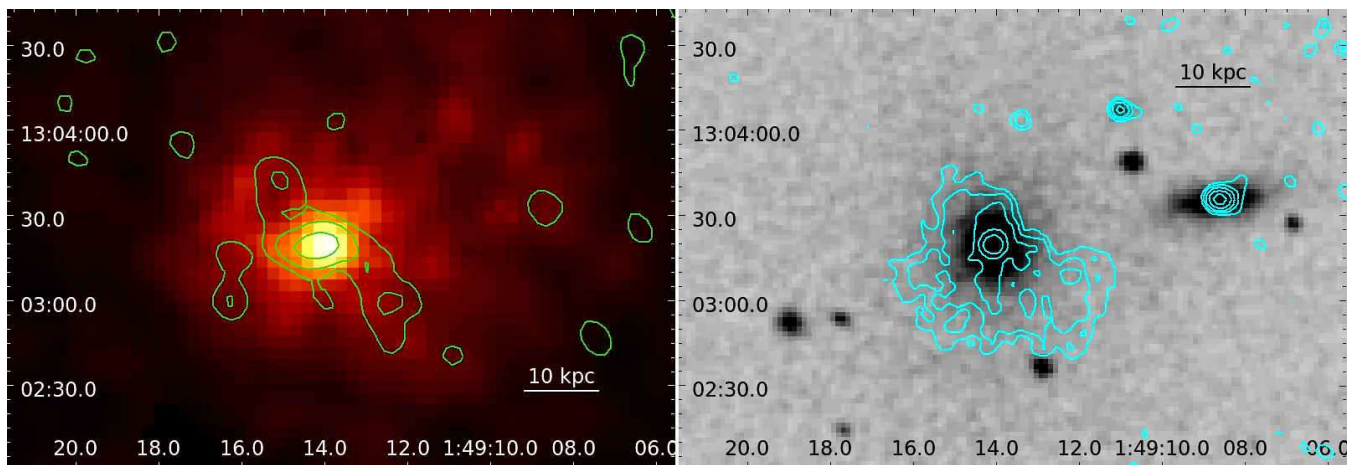


Figure A3. LGG 31 / NGC 677. *Left:* GMRT 235 MHz contours in green ($1\sigma = 1.2 \text{ mJy beam}^{-1}$), overlaid on the adaptively smoothed 0.3–2.0 keV *XMM-Newton* image. *Right:* GMRT 610 MHz contours in cyan ($1\sigma = 40 \mu\text{Jy beam}^{-1}$), overlaid on the *DSS* optical image. In both panels the radio contours are spaced by a factor of two, starting from 3σ . For this source the scale is $0.378 \text{ kpc arcsec}^{-1}$.

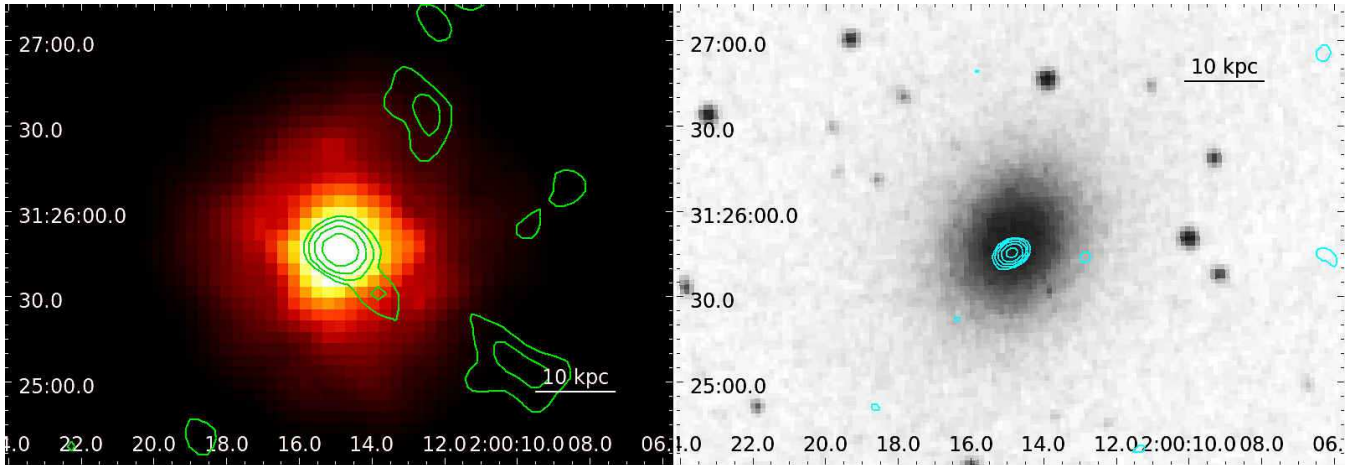


Figure A4. LGG 42 / NGC 777. *Left:* GMRT 235 MHz contours in green ($1\sigma = 0.4 \text{ mJy beam}^{-1}$), overlaid on the adaptively smoothed 0.3–2.0 keV *XMM-Newton* image. *Right:* GMRT 610 MHz contours in cyan ($1\sigma = 150 \mu\text{Jy beam}^{-1}$), overlaid on the *DSS* optical image. In both panels the radio contours are spaced by a factor of two, starting from 3σ . For this source the scale is $0.354 \text{ kpc arcsec}^{-1}$.

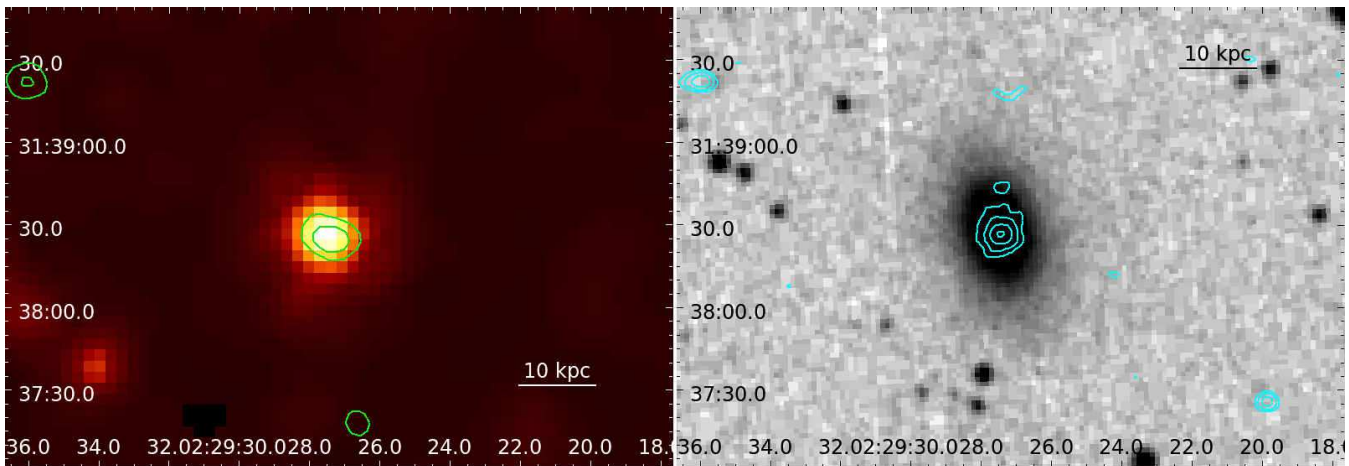


Figure A5. LGG 58 / NGC 940. *Left:* GMRT 235 MHz contours in green ($1\sigma = 0.3 \text{ mJy beam}^{-1}$), overlaid on the adaptively smoothed 0.3–2.0 keV *XMM-Newton* image. *Right:* GMRT 610 MHz contours in cyan ($1\sigma = 60 \mu\text{Jy beam}^{-1}$), overlaid on the *DSS* optical image. In both panels the radio contours are spaced by a factor of two, starting from 3σ . For this source the scale is $0.354 \text{ kpc arcsec}^{-1}$.

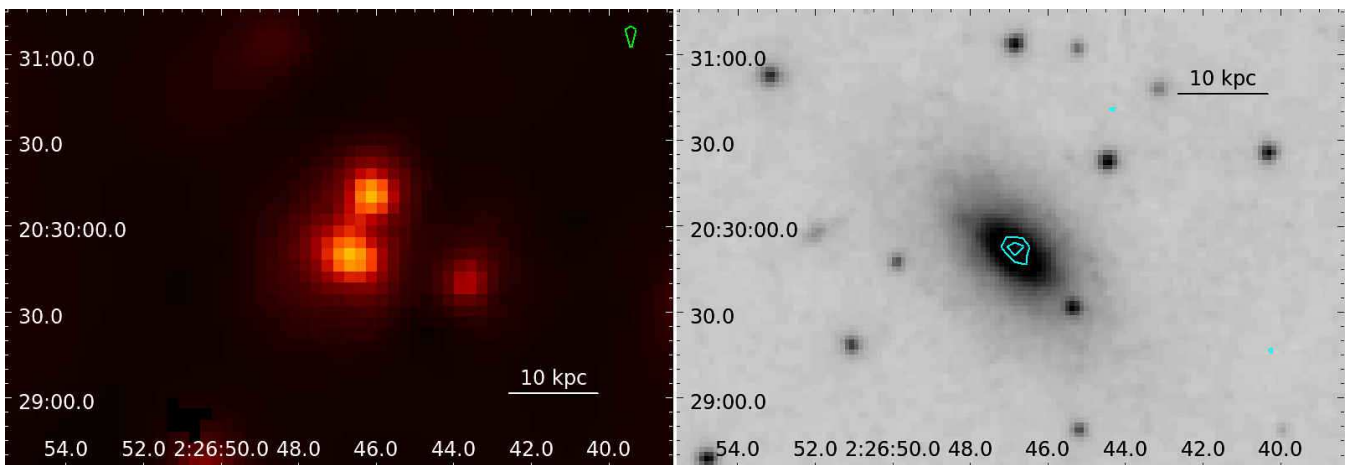


Figure A6. LGG 61 / NGC 924. *Left:* GMRT 235 MHz contours in green ($1\sigma = 0.3 \text{ mJy beam}^{-1}$), overlaid on the adaptively smoothed 0.3–2.0 keV *XMM-Newton* image. *Right:* GMRT 610 MHz contours in cyan ($1\sigma = 50 \mu\text{Jy beam}^{-1}$), overlaid on the *DSS* optical image. In both panels the radio contours are spaced by a factor of two, starting from 3σ . For this source the scale is $0.310 \text{ kpc arcsec}^{-1}$.

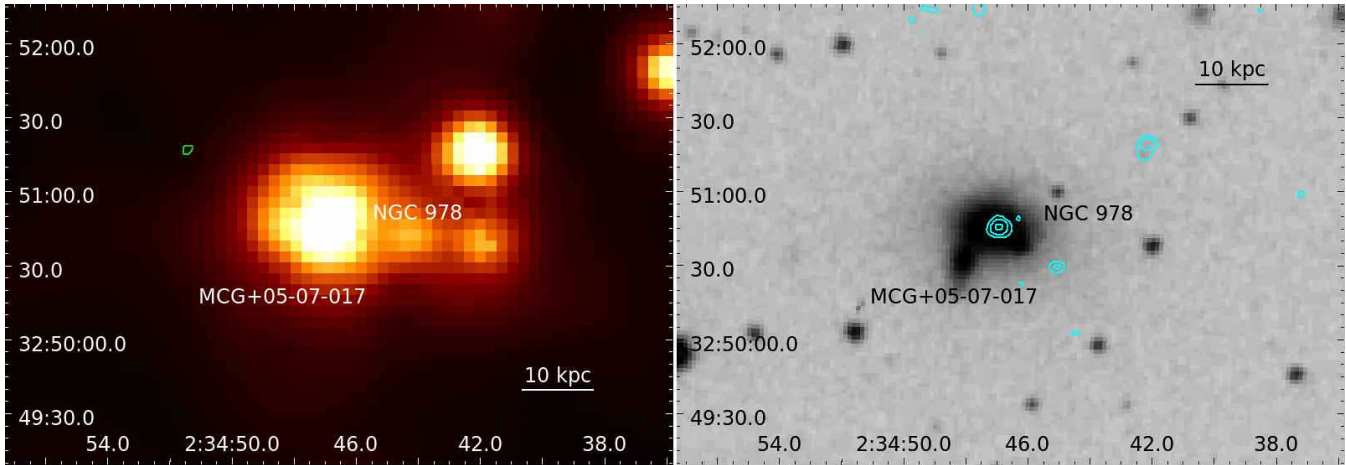


Figure A7. LGG 66 / NGC 978. *Left:* GMRT 235 MHz contours in green ($1\sigma = 0.4 \text{ mJy beam}^{-1}$), overlaid on the adaptively smoothed 0.3–2.0 keV *XMM-Newton* image. *Right:* GMRT 610 MHz contours in cyan ($1\sigma = 60 \mu\text{Jy beam}^{-1}$), overlaid on the *DSS* optical image. In both panels the radio contours are spaced by a factor of two, starting from 3σ . For this source the scale is $0.334 \text{ kpc arcsec}^{-1}$.

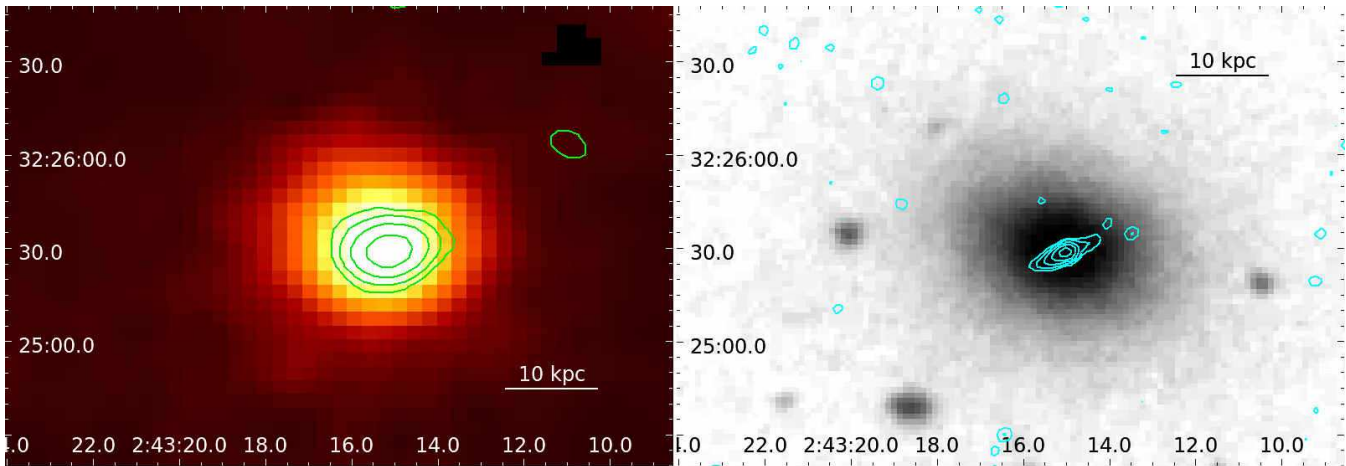


Figure A8. LGG 72 / NGC 1060. *Left:* GMRT 235 MHz contours in green ($1\sigma = 0.5 \text{ mJy beam}^{-1}$), overlaid on the adaptively smoothed 0.3–2.0 keV *XMM-Newton* image. *Right:* GMRT 610 MHz contours in cyan ($1\sigma = 90 \mu\text{Jy beam}^{-1}$), overlaid on the *DSS* optical image. In both panels the radio contours are spaced by a factor of two, starting from 3σ . For this source the scale is $0.368 \text{ kpc arcsec}^{-1}$.

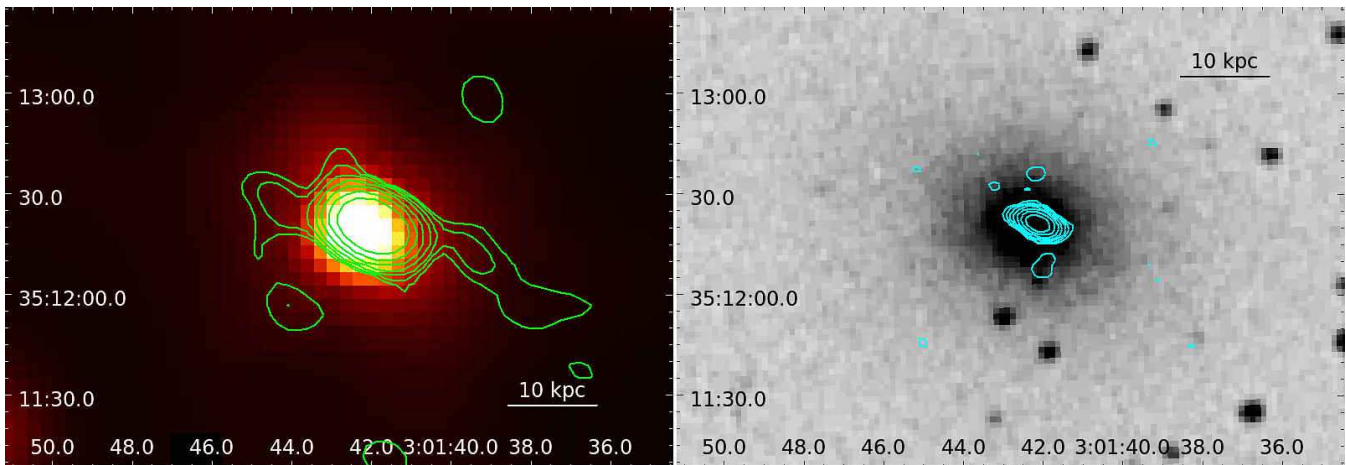


Figure A9. LGG 80 / NGC 1167. *Left:* GMRT 235 MHz contours in green ($1\sigma = 0.6 \text{ mJy beam}^{-1}$), overlaid on the adaptively smoothed 0.3–2.0 keV *XMM-Newton* image. *Right:* GMRT 610 MHz contours in cyan ($1\sigma = 60 \mu\text{Jy beam}^{-1}$), overlaid on the *DSS* optical image. In both panels the radio contours are spaced by a factor of two, starting from 3σ . For this source the scale is $0.349 \text{ kpc arcsec}^{-1}$.

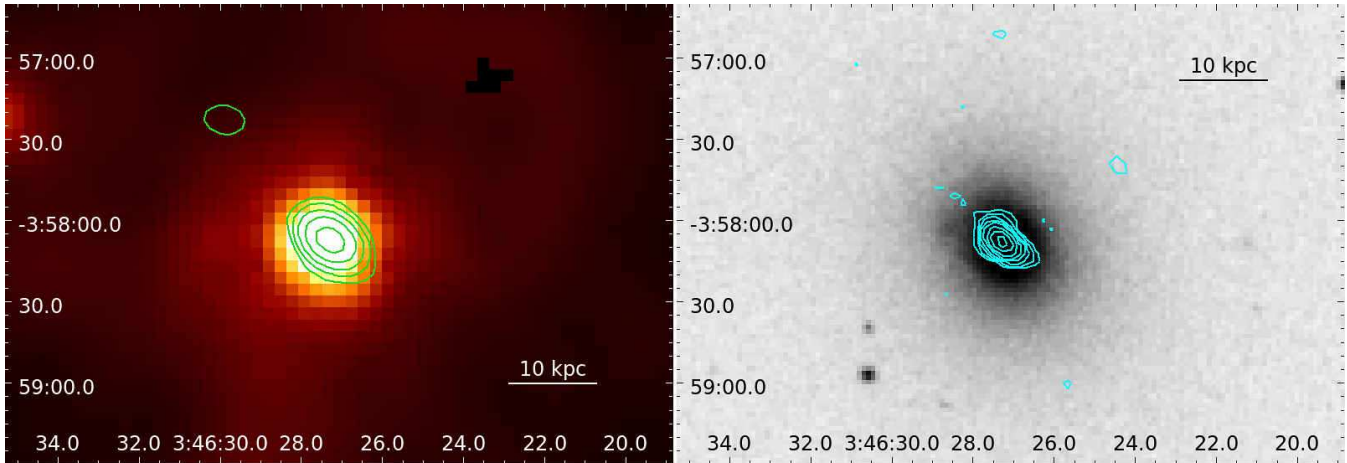


Figure A10. LGG 103 / NGC 1453. *Left:* GMRT 235 MHz contours in green ($1\sigma = 0.6 \text{ mJy beam}^{-1}$), overlaid on the adaptively smoothed 0.3–2.0 keV *XMM-Newton* image. *Right:* GMRT 610 MHz contours in cyan ($1\sigma = 60 \mu\text{Jy beam}^{-1}$), overlaid on the *DSS* optical image. In both panels the radio contours are spaced by a factor of two, starting from 3σ . For this source the scale is $0.305 \text{ kpc arcsec}^{-1}$.

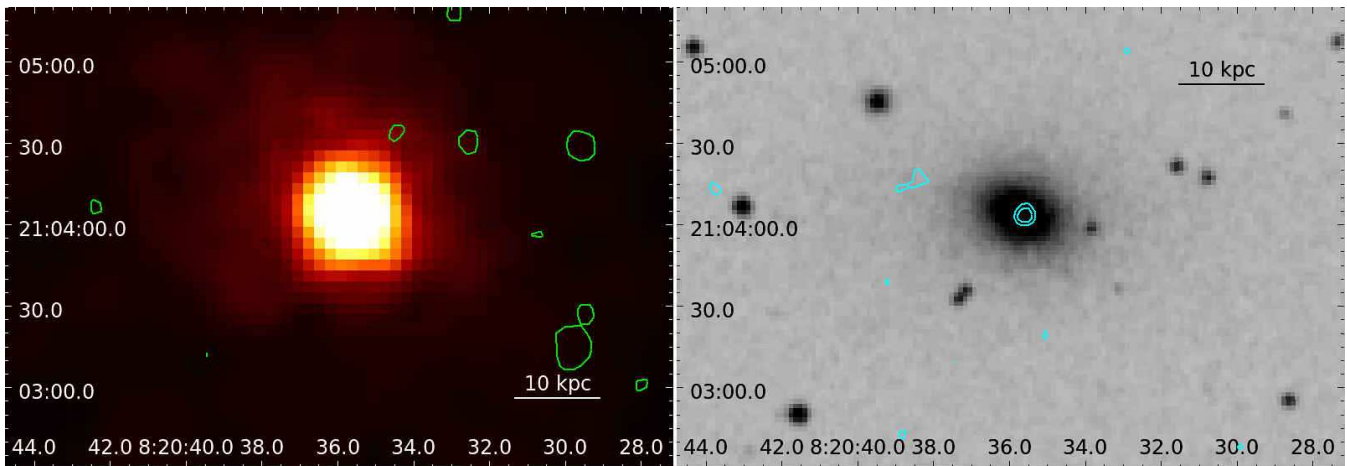


Figure A11. LGG 158 / NGC 2563. *Left:* GMRT 235 MHz contours in green ($1\sigma = 0.3 \text{ mJy beam}^{-1}$), overlaid on the adaptively smoothed 0.3–2.0 keV *XMM-Newton* image. *Right:* GMRT 610 MHz contours in cyan ($1\sigma = 70 \mu\text{Jy beam}^{-1}$), overlaid on the *DSS* optical image. In both panels the radio contours are spaced by a factor of two, starting from 3σ . For this source the scale is $0.315 \text{ kpc arcsec}^{-1}$.

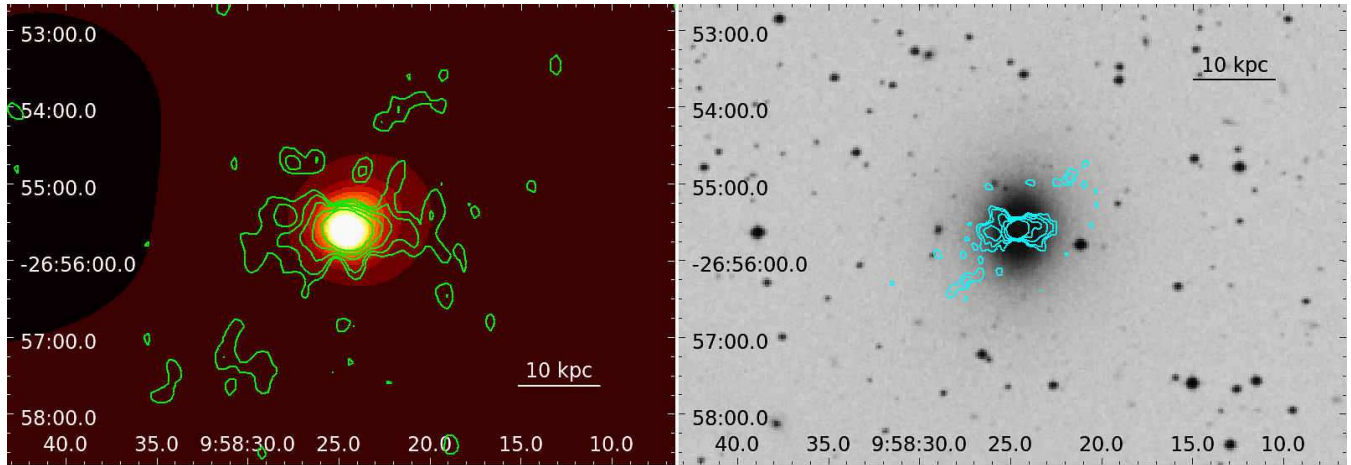


Figure A12. LGG 185 / NGC 3078. *Left:* GMRT 235 MHz contours in green ($1\sigma = 0.5 \text{ mJy beam}^{-1}$), overlaid on the adaptively smoothed 0.3–2.0 keV *Chandra* image. *Right:* GMRT 610 MHz contours in cyan ($1\sigma = 200 \mu\text{Jy beam}^{-1}$), overlaid on the *DSS* optical image. In both panels the radio contours are spaced by a factor of two, starting from 3σ . For this source the scale is $0.165 \text{ kpc arcsec}^{-1}$.

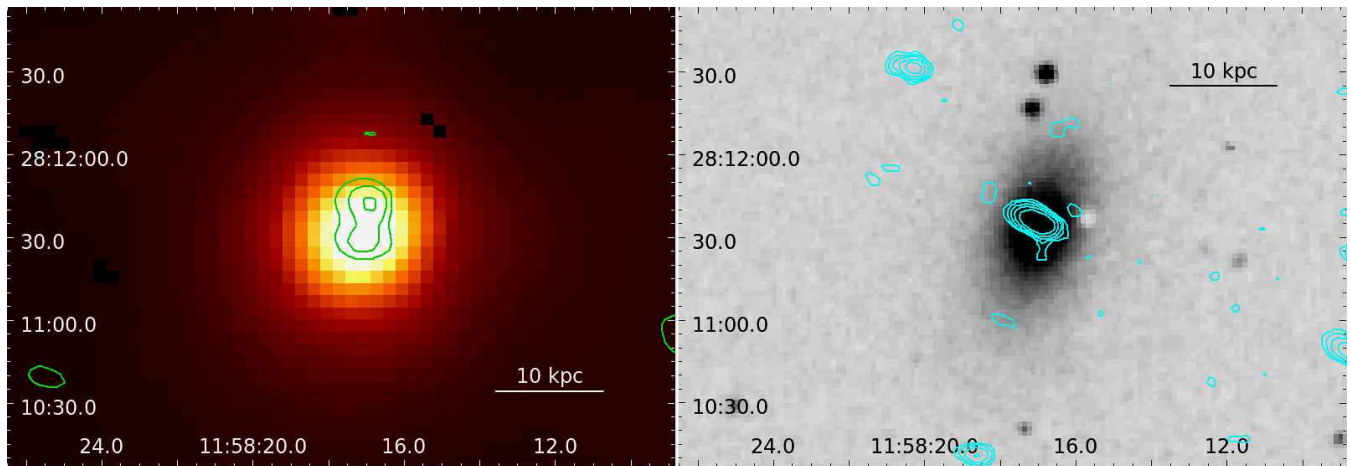


Figure A13. LGG 262 / NGC 4008. *Left:* GMRT 235 MHz contours in green ($1\sigma = 1.3 \text{ mJy beam}^{-1}$), overlaid on the adaptively smoothed 0.3–2.0 keV *XMM-Newton* image. *Right:* GMRT 610 MHz contours in cyan ($1\sigma = 50 \mu\text{Jy beam}^{-1}$), overlaid on the *DSS* optical image. In both panels the radio contours are spaced by a factor of two, starting from 3σ . For this source the scale is $0.262 \text{ kpc arcsec}^{-1}$.

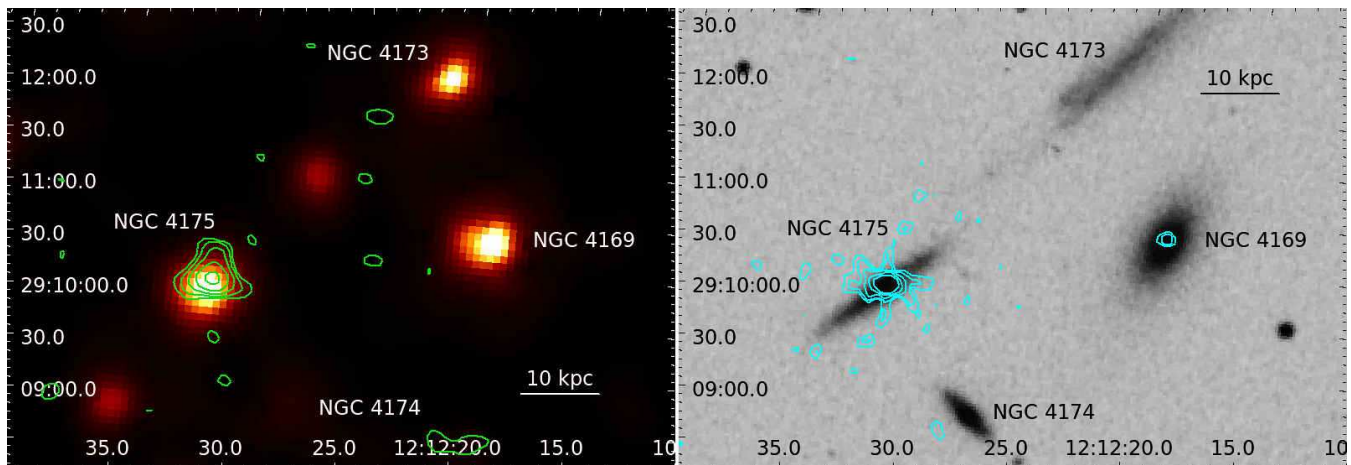


Figure A14. LGG 276 / NGC 4169. *Left:* GMRT 235 MHz contours in green ($1\sigma = 1.2 \text{ mJy beam}^{-1}$), overlaid on the adaptively smoothed 0.3–2.0 keV *XMM-Newton* image. *Right:* GMRT 610 MHz contours in cyan ($1\sigma = 80 \mu\text{Jy beam}^{-1}$), overlaid on the *DSS* optical image. In both panels the radio contours are spaced by a factor of two, starting from 3σ . For this source the scale is $0.218 \text{ kpc arcsec}^{-1}$.

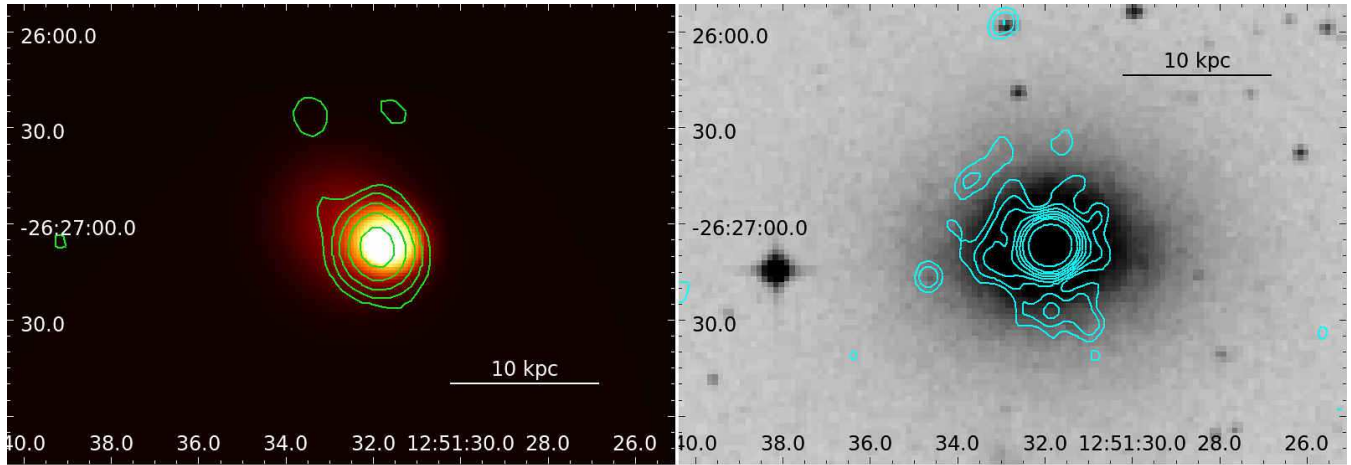


Figure A15. LGG 310 / ESO 507-25. *Left:* GMRT 235 MHz contours in green ($1\sigma = 0.5 \text{ mJy beam}^{-1}$), overlaid on the adaptively smoothed 0.3–2.0 keV *Chandra* image. *Right:* GMRT 610 MHz contours in cyan ($1\sigma = 100 \mu\text{Jy beam}^{-1}$), overlaid on the *DSS* optical image. In both panels the radio contours are spaced by a factor of two, starting from 3σ . For this source the scale is $0.218 \text{ kpc arcsec}^{-1}$.

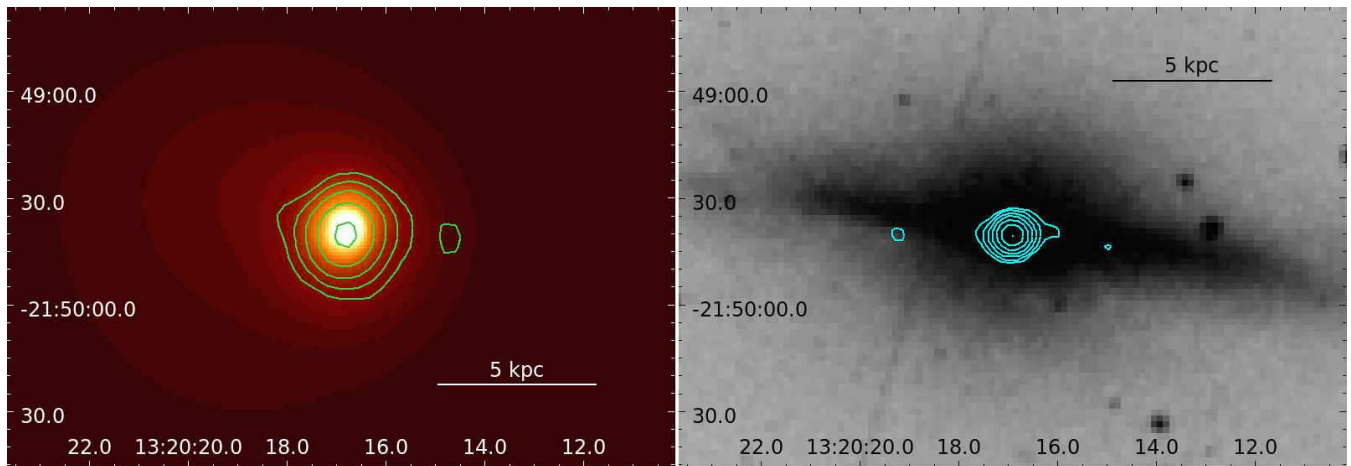


Figure A16. LGG 345 / NGC 5084. *Left:* GMRT 235 MHz contours in green ($1\sigma = 0.65 \text{ mJy beam}^{-1}$), overlaid on the adaptively smoothed 0.3–2.0 keV *Chandra* image. *Right:* GMRT 610 MHz contours in cyan ($1\sigma = 90 \mu\text{Jy beam}^{-1}$), overlaid on the *DSS* optical image. In both panels the radio contours are spaced by a factor of two, starting from 3σ . For this source the scale is $0.112 \text{ kpc arcsec}^{-1}$.

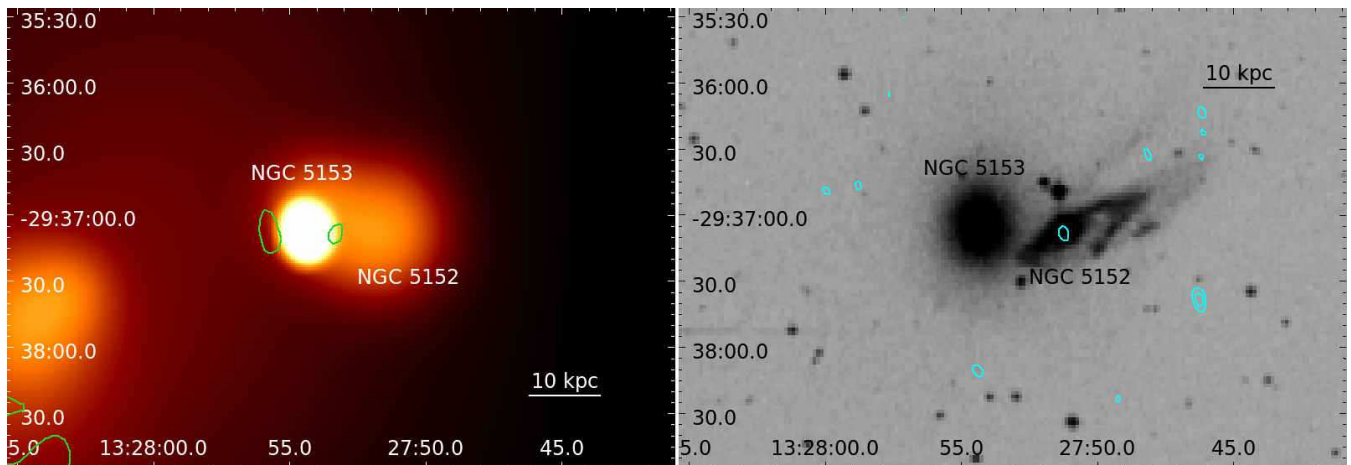


Figure A17. LGG 351 / NGC 5153. *Left:* GMRT 235 MHz contours in green ($1\sigma = 0.3 \text{ mJy beam}^{-1}$), overlaid on the adaptively smoothed 0.3–2.0 keV *Chandra* image. *Right:* GMRT 610 MHz contours in cyan ($1\sigma = 60 \mu\text{Jy beam}^{-1}$), overlaid on the *DSS* optical image. In both panels the radio contours are spaced by a factor of two, starting from 3σ . For this source the scale is $0.291 \text{ kpc arcsec}^{-1}$.

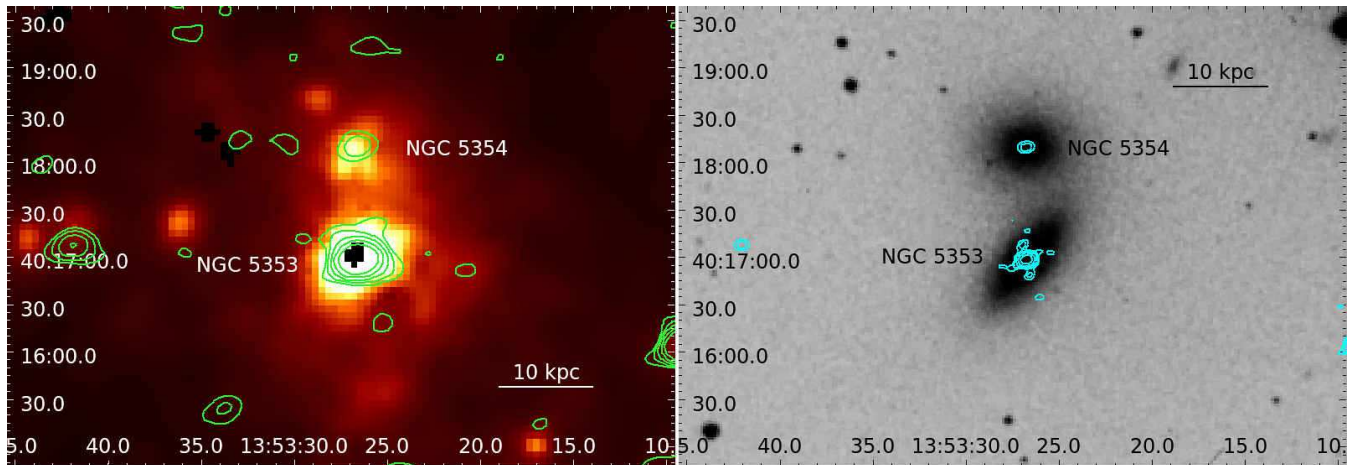


Figure A18. LGG 363 / NGC 5353. *Left:* GMRT 235 MHz contours in green ($1\sigma = 0.6 \text{ mJy beam}^{-1}$), overlaid on the adaptively smoothed 0.3–2.0 keV *XMM-Newton* image. *Right:* GMRT 610 MHz contours in cyan ($1\sigma = 60 \mu\text{Jy beam}^{-1}$), overlaid on the *DSS* optical image. In both panels the radio contours are spaced by a factor of two, starting from 4σ . For this source the scale is $0.170 \text{ kpc arcsec}^{-1}$.

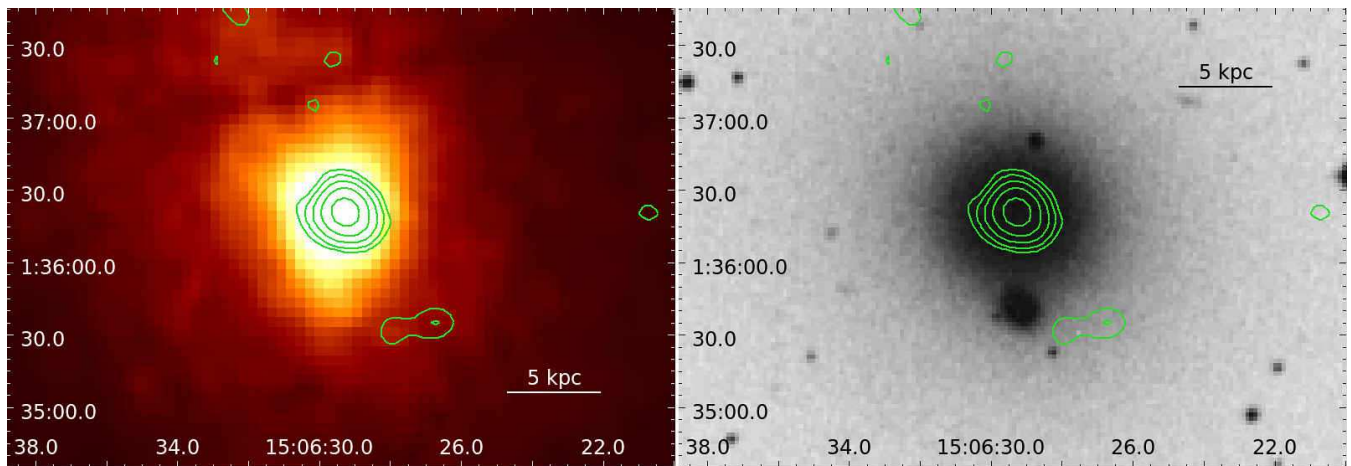


Figure A19. LGG 393 / NGC 5846. GMRT 235 MHz contours in green ($1\sigma = 0.5 \text{ mJy beam}^{-1}$), overlaid on the adaptively smoothed 0.3–2.0 keV *XMM-Newton* image (left) and on the *DSS* optical image (right). In both panels the radio contours are spaced by a factor of two, starting from 3σ . For this source the scale is $0.126 \text{ kpc arcsec}^{-1}$. X-ray cavities have been identified by Allen et al. (2006) and confirmed by Dong et al. (2010) at a distance $< 1 \text{ kpc}$ from the group centre. The low resolution of the 235 MHz image does not permit for a direct comparison as the X-ray cavities are placed in the central area covered by the radio point source.

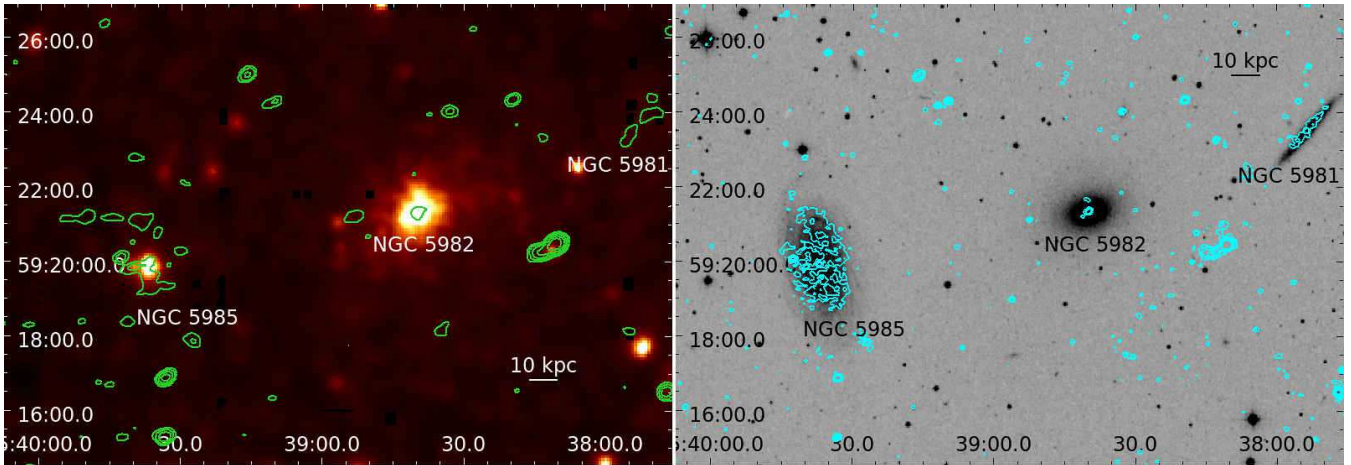


Figure A20. LGG 402 / NGC 5982 *Left:* GMRT 235 MHz contours in green ($1\sigma = 0.4 \text{ mJy beam}^{-1}$), overlaid on the adaptively smoothed 0.3–2.0 keV *XMM-Newton* image. *Right:* GMRT 610 MHz contours in cyan ($1\sigma = 90 \mu\text{Jy beam}^{-1}$), overlaid on the *DSS* optical image. In both panels the radio contours are spaced by a factor of two, starting from 3σ . For this source the scale is $0.213 \text{ kpc arcsec}^{-1}$.

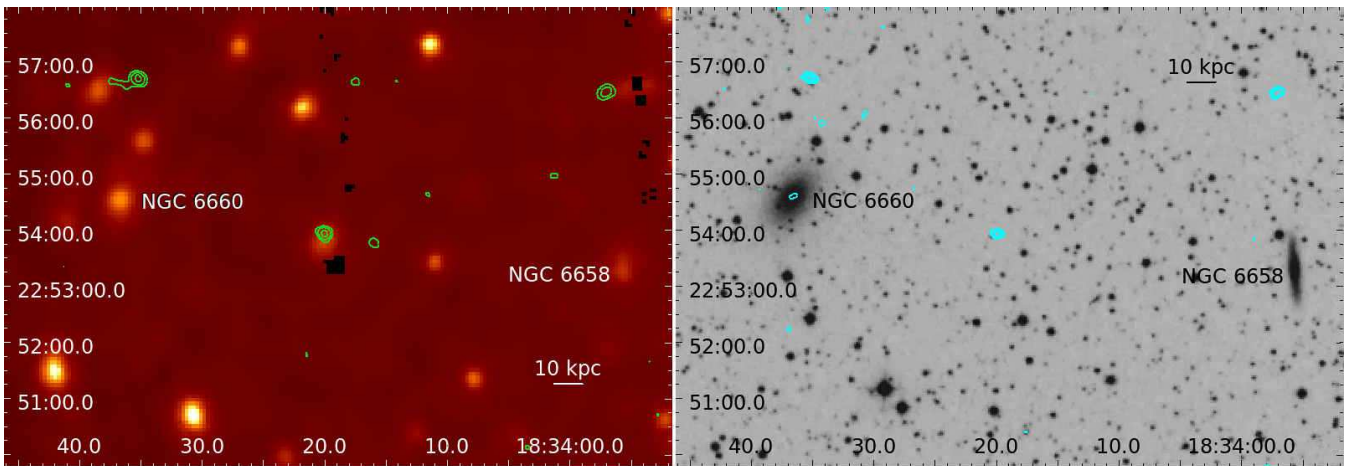


Figure A21. LGG 421 / NGC 6658. *Left:* GMRT 235 MHz contours in green ($1\sigma = 0.6 \text{ mJy beam}^{-1}$), overlaid on the adaptively smoothed 0.3–2.0 keV *XMM-Newton* image. *Right:* GMRT 610 MHz contours in cyan ($1\sigma = 50 \mu\text{Jy beam}^{-1}$), overlaid on the *DSS* optical image. In both panels the radio contours are spaced by a factor of two, starting from 3σ . For this source the scale is $0.305 \text{ kpc arcsec}^{-1}$.

APPENDIX B: STAR FORMATION RATES AND EXPECTED RADIO POWERS

Table B1 lists the FUV SFR for those galaxies where star formation could potentially affect our radio flux density measurements, and its estimated contribution to 610 MHz radio power.

Table B1. Star formation rates from FUV and the expected radio power at 610 MHz due to star formation for diffuse and point radio sources in our sample with FUV data. For each group we note the SFR_{FUV} , the expected radio power at 610 MHz $P_{610 \text{ expected}}$ from the calculated SFR_{FUV} , the radio power at 610 MHz $P_{610 \text{ observed}}$, and the radio morphology of the source.

| Group LGG | BGE | SFR_{FUV} ($10^{-2} M_{\odot} \text{ yr}^{-1}$) | $P_{610 \text{ expected}}$ ($10^{21} \text{ W Hz}^{-1}$) | $P_{610 \text{ observed}}$ ($10^{21} \text{ W Hz}^{-1}$) | Morphology |
|--------------|------------|--|---|---|------------|
| 18 | NGC 410 | 7.5 | 0.26 | 9.6 | point |
| 27 | NGC 584 | 1.3 | 0.05 | 0.08 ^a | point |
| 31 | NGC 677 | 3.4 | 0.12 | 33.1 | diffuse |
| 42 | NGC 777 | 9.3 | 0.33 | 6.5 | point |
| 58 | NGC 940 | 9.8 | 0.34 | 2.8 | point |
| 61 | NGC 924 | 4.8 | 0.17 | 0.8 | point |
| 66 | NGC 978 | 2.2 | 0.08 | 0.7 | point |
| 103 | NGC 1453 | 2.7 | 0.09 | 19.0 | point |
| 117 | NGC 1587 | 2.2 | 0.08 | 69.2 | diffuse |
| 158 | NGC 2563 | 4.1 | 0.15 | 0.7 | point |
| 185 | NGC 3078 | 1.4 | 0.05 | 52.9 | diffuse |
| 262 | NGC 4008 | 1.7 | 0.06 | 5.7 | point |
| 310 | ESO 507-25 | 11.1 | 0.39 | 11.2 | diffuse |
| 345 | NGC 5084 | 1.8 | 0.07 | 2.3 | point |
| 363 | NGC 5353 | 3.9 | 0.14 | 6.7 | point |
| 402 | NGC 5982 | 4.5 | 0.16 | 0.4 | point |
| 473 | NGC 7619 | 3.1 | 0.11 | 11.2 | point |

^a $P_{610 \text{ observed}}$ was calculated here by extrapolating the 610 MHz flux density from the available 1.4 GHz emission, using a spectral index of 0.8

APPENDIX C: RADIO SPECTRA OF CLOGS BGES

Figure C shows the radio spectra of the BGEs detected at 235, 610 and 1400 MHz.

This paper has been typeset from a $\text{\TeX}/\text{\LaTeX}$ file prepared by the author.

Figure C1. Flux density distribution of CLoGS central galaxies over 235, 610 and 1400 MHz

